Soil moisture content retrieval over meadows from Sentinel-1 and Sentinel-2 data using physically based scattering models

Harm-Jan F. Benninga [*,1], Rogier van der Velde, Zhongbo Su

Department of Water Resources, Faculty of Geo-Information Science and Earth Observation (ITC), University of Twente, P.O. Box 217, Enschede, 7500 AE, The Netherlands

ARTICLE INFO

ABSTRACT

Soil moisture content (SMC) information at field scale could have important applications in agricultural and regional water management. This study presents an operationally applicable scheme for SMC retrieval over meadows from synthetic aperture radar (SAR) backscatter (σ^0) observations. We parameterized the vegetation scattering and absorption model developed at the Tor Vergata University of Rome (TV) and the integral equation method (IEM) surface scattering model for grass-covered soil surfaces. Leaf area index (LAI) estimates from a Sentinel-2 product provide field-scale vegetation information, as is demonstrated by validation against in situ measurements. The SMC retrieval scheme is applied with field-averaged Sentinel-1 σ^0 observations from November 2015 to November 2018 and evaluated on 21 meadows against adjacent in situ station measurements, without (IEM) and with a vegetation correction (TV-IEM). Masking the IEM and TV-IEM SMC retrievals for dense vegetation conditions improves their performance, but this is a trade-off with the number of retrievals. By setting the SMC retrievals that exceed the upper retrieval limit of $0.75\,\mathrm{m^3\,m^{-3}}$ during the wet period to the maximum SMC, the performance metrics improve to mean Pearson correlation coefficients of 0.55 for IEM and 0.64 for TV-IEM, root mean square deviations ($RMSD$) of $0.14\,\mathrm{m^3\,m^{-3}}$ for IEM and $0.13\,\mathrm{m^3\,m^{-3}}$ for TV-IEM, and $RMSD$s relative to the range of the SMC references of $24\,\%$ for both IEM and TV-IEM. The slightly better SMC retrieval performance with TV-IEM is caused by invalid SMC retrievals under dense vegetation conditions, and the performance metrics for IEM and TV-IEM are practically equal by considering the same retrieval–reference pairs. The IEM and TV-IEM retrieval performances are also similar to the performances of two other Sentinel-1 based products at field scale. They are, on average, outperformed by NASA's Soil Moisture Active Passive (SMAP) $9\,\mathrm{km}$ and $36\,\mathrm{km}$ products evaluated at field scale, but these products are expected to deviate if larger regional differences are present and in field-specific situations.

1. Introduction

Microwave backscatter (σ^0) observations by synthetic aperture radar (SAR) instruments are known for their potential to monitor soil moisture content (SMC). Recently, interest has grown in the Sentinel-1 satellites because of the combination of its fine spatiotemporal resolutions, high radiometric accuracy and the operational ambition of the programme (Balenzano et al., 2021; Bauer-Marschallinger et al., 2019; Hornacek et al., 2012; Pulvirenti et al., 2018). Balenzano et al. (2021), Bauer-Marschallinger et al. (2019) and Pulvirenti et al. (2018) developed algorithms for the retrieval of SMC from Sentinel-1 observations at resolutions of $1\,\mathrm{km}$, $1\,\mathrm{km}$ and $500\,\mathrm{m}$, respectively.

Several studies noted the potential of Sentinel-1 σ^0 observations for monitoring SMC even at finer scales, up to agricultural field scale (e.g.

Amazirh et al., 2018; El Hajj et al., 2017). Especially over heterogeneous landscapes with relatively small agricultural fields, such as in western Europe, new applications may be anticipated with SMC information at field scale. This includes agricultural water management for field trafficability and irrigation (Carranza et al., 2019; Lei et al., 2020; Vereecken et al., 2014), and regional catchment management in dry and wet periods (Cenci et al., 2017; Mahanama et al., 2008; Pauwels et al., 2001; Pezij et al., 2019).

For the SMC to be estimated from Sentinel-1 observations, the relation between σ^0 and SMC must be separated from the effects of surface roughness and vegetation (Kornelsen and Coulibaly, 2013; Paloscia et al., 2013; Verhoest et al., 2008). Surface scattering models, such as the frequently-used 'integral equation method' (IEM) model, simulate the σ^0 from surfaces based on the surface roughness and SMC

(via relative permittivity) given the sensing configurations regarding frequency and incidence angle (Ulaby and Long, 2014). The surface roughness of meadows is expected to change little because typically no crop rotation and ploughing are applied. In addition, the absence of a clear row structure — from ploughing or other agricultural practices — suggests that satellite σ^0 observations from the ascending and descending passes, despite the different directions from which fields are viewed, may be combined. The results in Benninga et al. (2020) confirm that the IEM surface roughness parameters can be assumed similar for different meadows, time-invariant and independent of the ascending/descending orbits. This is a promising finding for the retrieval of SMC over meadows across a larger region because it suggests that using a single set of surface roughness parameters would be allowed. The value of such a product would be substantial as meadows cover a major portion of the land in use for agriculture. However, this finding was obtained only for two meadows. Furthermore, the meadows were in relatively wet and sparsely vegetated (winter) conditions. Hence, further research is required over additional meadows and for a range of hydrometeorological and vegetation conditions.

The development of vegetation throughout a year complicates the retrieval of SMC. Interactions of the microwave signal with vegetation results in attenuation of the soil σ^0, direct σ^0 from the vegetation and σ^0 from soil–vegetation pathways (Ulaby and Long, 2014). These effects are enhanced by Sentinel-1's sub-optimal specifications for SMC retrieval, notably the C-band (wavelength 5.6 cm) observations at relatively large incidence angles and in VV polarization (Fascetti et al., 2017; Pulvirenti et al., 2018). Based on the theory it is, thus, expected that correcting Sentinel-1 σ^0 observations for vegetation effects contributes to more accurate SMC retrievals. The discrete electromagnetic Tor Vergata (TV) model coupled with the IEM surface scattering model (Bracaglia et al., 1995; Dente et al., 2014; Wang et al., 2018) is a physically based model. Advantages of using a physically based model are the application to various site conditions and sensor configurations (Paloscia et al., 2013; Petropoulos et al., 2015) as well as propagation of uncertainty sources (Benninga et al., 2020; Satalino et al., 2002; Van der Velde et al., 2012) and the understanding of backscattering processes (Baghdadi et al., 2002; Balenzano et al., 2012; Wang et al., 2018). However, deficiencies in the models, their parameterizations and uncertainty in the input variables, such as current vegetation conditions, will influence the accuracy of SMC retrievals and the effectiveness of a vegetation correction on improving SMC retrieval performance.

This study presents an operationally applicable scheme for SMC retrieval over meadows. In this context, it extends on previous research by (i) using physically based model simulations for field-scale SMC retrieval from SAR σ^0 observations and (ii) evaluating the effectiveness of correction for the effect of vegetation as a balance between a better representation of scattering processes and the uncertainty added by imperfect models as well as the inclusion of more parameters and input variables. The operationally applicable scheme is established by the Sentinel-1 and Sentinel-2 programmes with operational ambitions, input data sets of land cover and soil texture that are regionally available and have global alternatives, use of physically based models with a limited number of parameters and the parameters being available from other sources, and look-up tables of the model simulations for fast inversion into SMC. We parameterized the TV and IEM models for grass-covered soil surfaces. For representing field-scale vegetation conditions, we utilized a leaf area index (LAI) product derived from Sentinel-2 optical imagery (Paepen and Wens, 2017; VITO, 2019). The Sentinel-2 LAI estimates were validated against in situ measurements collected on six agricultural fields in the east of the Netherlands. The parameters required for the TV and IEM models were adopted from previous studies, except for the vegetation water content (VWC) for which various time-invariant and time-varying VWC values were tested. Then, the SMC retrieval scheme was demonstrated by retrieving the SMC from Sentinel-1 σ^0 observations for 21 meadows and validated

against measurements from adjacent in situ monitoring stations. To evaluate whether the vegetation correction improves the SMC estimates, the retrieval results with IEM (without vegetation correction) and TV-IEM (with vegetation correction) were compared. Besides, we tested whether the performance improves by incorporating information from SMC retrievals that exceed the upper SMC retrieval limit and by masking SMC retrievals for dense vegetation conditions. Eventually, the SMC retrieval performances were compared with the performances of three other Sentinel-1 based products at field scale, three Sentinel-1 based products at 1 km resolution and the Soil Moisture Active Passive (SMAP) 9 km and 36 km products evaluated at field scale.

2. Soil moisture content retrieval scheme

Fig. 1 shows the SMC retrieval scheme, separated in the boxes A–C.

2.1. A: Input data

The preparation of the input data starts with the selection of meadows within a study region. In case of the Netherlands this can be done with the crop parcel registry ('Basisregistratie Gewaspercelen' in Dutch; Ministry of Economic Affairs and Climate Policy, 2020). This database contains, on an annual basis, the type of crop for each agricultural parcel in the Netherlands. For the selected meadows the average soil texture, Sentinel-1 σ^0 and incidence angle, and Sentinel-2 LAI were calculated. For the soil texture we could use the soil physical properties map of the Netherlands (BOFEK2012; Wösten et al., 2013). Besides regional data sets, global alternatives for providing land cover and soil texture are the 10 m resolution WorldCover map (VITO, 2022) and the 30′ Harmonized World Soil Database (FAO/IIASA/ISRIC/ISS-CAS/JRC, 2009). Below, the preparation steps that were applied to the Sentinel-1 imagery and Sentinel-2 LAI maps are described.

2.1.1. Sentinel-1 imagery

Sentinel-1 σ^0 and local incidence angle values for study fields were obtained from Level-1 Ground Range Detected (GRD) High Resolution (HR) Interferometric Wide Swath (IW) imagery. The images were downloaded from the Copernicus Open Access Hub (Copernicus, 2019). The operations (1) Apply Orbit File, (2) Thermal Noise Removal and (3) Range Doppler Terrain Correction, including radiometric normalization to σ^0 (in m^2 m^{-2}) with projected local incidence angles, available in ESA's Sentinel Application Platform (SNAP) V6.0 (European Space Agency (ESA), 2019), were used to pre-process the Sentinel-1 images. If the SMC retrieval scheme would be utilized on areas with significant relief, a terrain flattening operation to γ^0 may be required. The study region here is almost flat (see Section 4.1) and these pre-processing steps were considered appropriate.

The Level-1 GRD HR IW Sentinel-1 images have, after multi-looking, a resolution of 20 m × 22 m (Bourbigot et al., 2016; Torres et al., 2012). The Range Doppler Terrain Correction included projection of the Sentinel-1 σ^0 and local incidence angles on a geographic grid (WGS84) with a pixel spacing of 9.0E−5° (equivalent to 10 m × 6.1 m at the study region's latitude). After the pre-processing operations the Sentinel-1 σ^0 and incidence angle values were averaged over study fields, excluding the area within 20 m from borders of fields and 40 m from trees and buildings to avoid possible influences from outside fields. The final steps were to mask the Sentinel-1 σ^0 observations of study fields for frozen conditions, wet snow and intercepted rain with the masking rules for weather-related surface conditions presented in Benninga et al. (2019) and to express the σ^0 intensity values in dB. The Sentinel-1 σ^0 observations still contain radiometric uncertainty due to calibration uncertainties, sensor instabilities and speckle (Benninga et al., 2019; Pathe et al., 2009; Schmidt et al., 2018; Schwerdt et al., 2017). The radiometric uncertainty follows approximately an inverse square root dependency on the surface area over which σ^0 observations are averaged (Benninga et al., 2019). Benninga et al. (2020) demonstrated
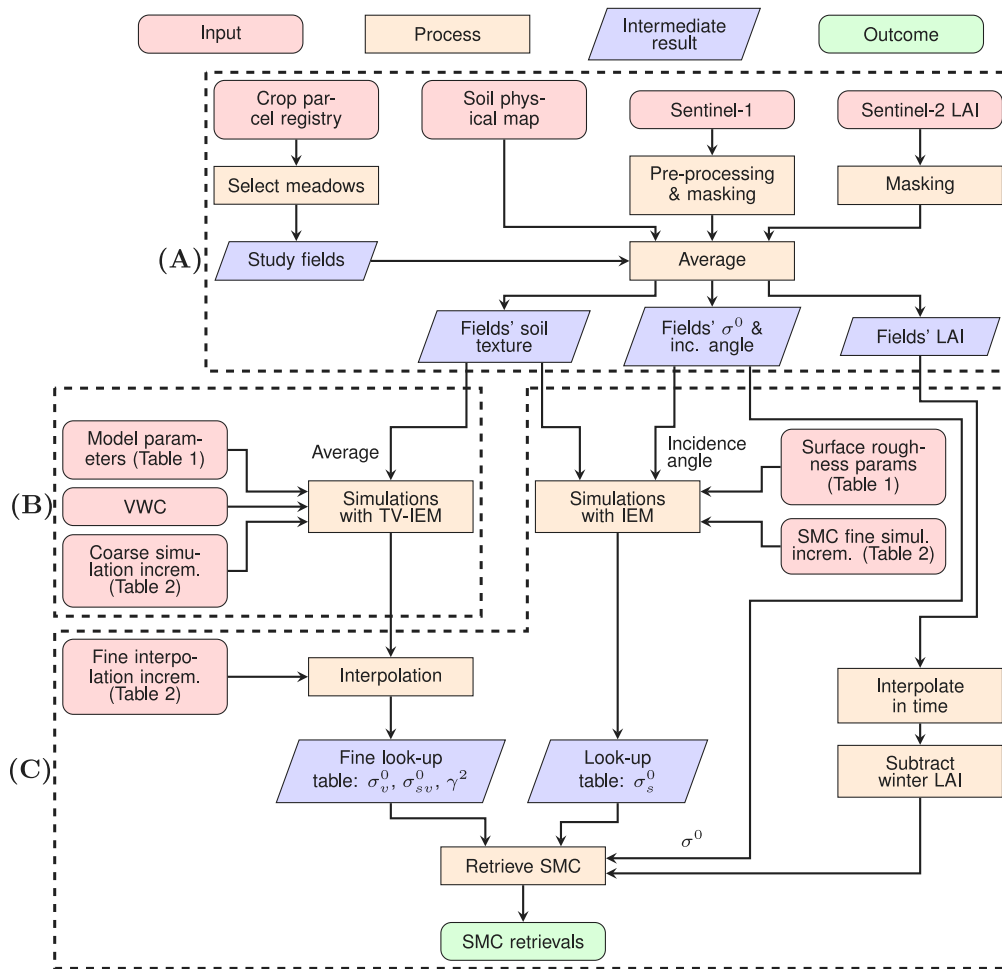
Fig. 1. Flowchart of the SMC retrieval scheme, separated in the preparation of the input data **(A)**, the parameterization of the TV-IEM model **(B)**, and the retrieval of SMC from σ^0 observations **(C)**.

that, averaged over three study fields of $0.45\,ha$ to $2.4\,ha$, Sentinel-1's radiometric uncertainty constitutes 31% of the retrieval uncertainty at a SMC of $0.26\,m^3\,m^{-3}$ to 67% at a SMC of $0.53\,m^3\,m^{-3}$.

The Sentinel-1 IW mode provides σ^0 observations in VV and VH polarization. The σ^0 observations in VV polarization have a higher expected sensitivity to SMC (e.g. Amazirh et al., 2018; El Hajj et al., 2017; Pulvirenti et al., 2018). Therefore, only the VV polarization σ^0 observations were used in the presented SMC retrieval scheme. The ascending and descending Sentinel-1 orbits were combined, as Benninga et al. (2020) found that σ^0 observations from these respective pass directions can be simulated with one set of surface roughness parameters over meadows. The Sentinel-1 constellation consists of the Sentinel-1A and Sentinel-1B satellites, which provide imagery since October 2014 and September 2016 (Bourbigot et al., 2016; Torres et al., 2012). Their imaging revisit time over the European landmasses, which is one of the high priority areas in Sentinel-1's acquisition strategy (Bauer-Marschallinger et al., 2019; Torres et al., 2012), is approximately 3 to 8 days with Sentinel-1A and improves to 1.5 to 3 days with both Sentinel-1A and -1B. Inconsistencies in the Sentinel-1 σ^0 time series are found before 25 November 2015 as a result of changes in Sentinel-1 calibrations (Benninga et al., 2019; El Hajj et al., 2016), so the SMC retrieval scheme was started from 25 November 2015 and it was continued until 1 November 2018.

2.1.2. Sentinel-2 leaf area index

The Sentinel-2A and -2B satellites provide imagery in 13 spectral bands in the visible, near infrared and short wave infrared parts of the electromagnetic spectrum (Drusch et al., 2012). The resolution is $10\,m$, $20\,m$ or $60\,m$, depending on the spectral band. The revisit time over the Netherlands is 12 to 6 days from 1 July 2015 to 1 July 2017 (Sentinel-2A) and 5 to 2.5 days from 1 July 2017 onwards (Sentinel-2A and Sentinel-2B).

Using Sentinel-2 imagery, the Flemish Institute for Technological Research ('Vlaamse Instelling voor Technologisch Onderzoek' in Dutch, or VITO) generates $10\,m$ grid maps of various vegetation indicators, namely the fraction of absorbed photosynthetically active radiation, fraction of green vegetation cover, LAI, normalized difference vegetation index (NDVI), chlorophyll canopy content and chlorophyll water content (Paepen and Wens, 2017; VITO, 2019). The maps are masked for the scene classifications cloud shadow, medium probability for clouds and high probability for clouds. For this study, V102 vegetation indicator maps as well as scene classification maps were downloaded from the VITO Product Distribution Portal (VITO, 2019). Recently, V200 replaced V102 and the distribution moved to Terrascope (Piccard et al., 2020). The Sentinel-2 LAI maps were available for parts of Europe (Paepen and Wens, 2017; VITO, 2019). A global alternative for LAI information, but at a coarser resolution of up to $250\,m$, is provided by the Moderate Resolution Imaging Spectroradiometer (MODIS) vegetation indicators (Justice et al., 2002; Xiao et al., 2022).

Fig. 2 illustrates that individual fields can be distinguished on the Sentinel-2 LAI maps. Differences between the LAI values of meadows exist due to different management practices: part of them is being grazed and others are cut at several moments in the year. On 15 September 2016 (the example map in Fig. 2) part of the crop fields had already been harvested, whereas on others the crop was still there.
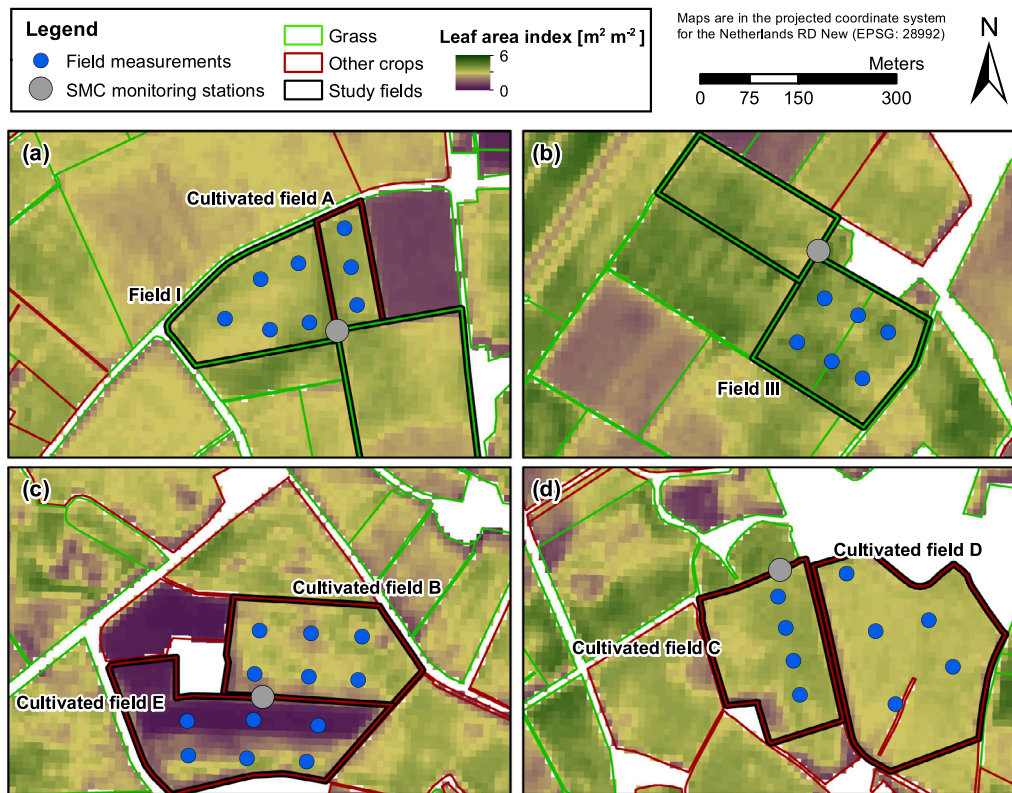
Fig. 2. Sentinel-2 LAI maps on 15 September 2016 for the fields where we collected in situ LAI measurements. The outlines of the agricultural fields originate from the crop parcel registry 2016 (Ministry of Economic Affairs and Climate Policy, 2020).

The Sentinel-2 LAI images are not collected at the same time as Sentinel-1 images. Furthermore, only about 40 % of the LAI estimates is available after the masking for cloud shadow, medium probability and high probability for clouds. To provide LAI information at the time of Sentinel-1 images we, therefore, had to interpolate the Sentinel-2 LAI estimates. We assumed that we do not have local information available, such as when a study field was sowed or harvested, to enable region-wide application of the Sentinel-2 LAI information. Instead, we linearly interpolated two subsequent Sentinel-2 LAI estimates if the time gap between them is less than 15 days and the LAI does not decrease more than $2\,m^2\,m^{-2}$, thereby assuming that a larger decrease associates with the harvesting of a crop. For the winter period between 1 November and 1 March no variation in LAI is expected and we adopted the mean of Sentinel-2 LAI estimates over this period for a field. Furthermore, if a Sentinel-1 observation is between two Sentinel-2 LAI estimates for which the time gap is larger than 15 days (i.e. no interpolated LAI estimate would be available for the Sentinel-1 observation), a maximum time gap of 1.5 days was taken for directly associating a Sentinel-2 LAI estimate to a Sentinel-1 observation. The interpolated Sentinel-2 LAI estimates are validated against in situ LAI measurements in Section 5.1.

2.2. B: Forward backscattering model

2.2.1. Surface and vegetation models

The total σ^0 constitutes of three contributions as follows (in $m^2\,m^{-2}$):

$$\sigma^0 = \gamma^2\sigma_s^0 + \sigma_v^0 + \sigma_{sv}^0, \tag{1}$$

where γ^2 is the two-way transmissivity of the vegetation (= 1−two-way attenuation), σ_s^0 is the σ^0 from the soil surface, σ_v^0 is the direct vegetation σ^0 and σ_{sv}^0 is the σ^0 from soil–vegetation pathways. The IEM surface scattering model (Fung et al., 1992) simulates the scattering

in all upward directions from the soil by representing it as a rough dielectric surface. The TV electromagnetic model, developed at the Tor Vergata University of Rome, represents the vegetation as a medium of discrete scatterers and simulates the γ^2, σ_v^0 and σ_{sv}^0 based on radiative transfer theory. Readers are referred to Bracaglia et al. (1995) and Dente et al. (2014) for more background on the TV-IEM model.

2.2.2. Parameterization

We implemented the TV model for grass-covered surfaces using the vegetation parameterization reported in Dente et al. (2014), excluding the litter layer, and the IEM surface roughness parameter values that were calibrated on sparsely vegetated meadows in Benninga et al. (2020). The vegetation leaves' disc radius and disc thickness were calibrated on an alpine meadow landscape (Dente et al., 2014). The TV vegetation and IEM surface roughness parameter values are listed in Table 1. For the soil texture parameters, we used the average sand, silt and clay content, and soil bulk density of the study fields (i.e. regional averages).

The LAI determines the number of discs that represent the vegetation (Bracaglia et al., 1995). In Benninga et al. (2020) it has been assumed that the sparse grass cover on meadows in winter conditions does not affect the Sentinel-1 σ^0 observations. To enable adopting the surface roughness parameter values from Benninga et al. (2020), we subtracted from the Sentinel-2 LAI estimates the LAI during winter before they were used as input to the SMC retrieval scheme.

Regarding the VWC vegetation variable, previous studies adopted time-invariant values of $0.8\,kg\,kg^{-1}$ (Dente et al., 2014) and $0.59\,kg\,kg^{-1}$ (Wang et al., 2018) for grass. These VWC values were obtained after optimizing TV simulations with regard to passive and active microwave observations over Tibetan alpine meadows. However, given the water-limited conditions that can occur in our study region, the VWC may vary over time as well. Therefore, besides searching for one optimum VWC value, we also investigated implementation of a

Table 1

The surface and vegetation parameters used for simulating a grass-covered soil surface with the TV-IEM model.

Module	Parameter	Symbol	Value	Source
Surface	Root mean square surface height	s	0.16 cm	Benninga et al. (2020)
Surface	Autocorrelation length	c_l	1.31 cm	Benninga et al. (2020)
Surface	Soil texture: sand, silt and clay content, and soil bulk density	-	Averages for the study fields, see Section 4.1	
Vegetation	Leaves' disc radius	R_{leaf}	1.4 cm	Dente et al. (2014)
Vegetation	Leaves' disc thickness	D_{leaf}	0.02 cm	Dente et al. (2014)

Table 2

Discretization of the TV-IEM look-up tables. Regarding LAI, the simulation nodes are $[0\,\mathrm{m^2\,m^{-2}},\ 1\,\mathrm{m^2\,m^{-2}},\ \ldots,\ 10\,\mathrm{m^2\,m^{-2}}]$ with an additional simulation for $0.1\,\mathrm{m^2\,m^{-2}}$. Regarding SMC, the simulations nodes are $[0.05\,\mathrm{m^3\,m^{-3}},\ 0.1\,\mathrm{m^3\,m^{-3}},\ \ldots,\ 0.75\,\mathrm{m^3\,m^{-3}}]$ with an additional simulation for $0.01\,\mathrm{m^3\,m^{-3}}$.

Variable	Lower limit	Upper limit	Coarse simulation increment	Fine interpolation increment
Incidence angle [°]	29	47	2	0.25
LAI [$\mathrm{m^2\,m^{-2}}$]	0, 0.1	10	1.0	0.1
VWC [$\mathrm{kg\,kg^{-1}}$]	0.4	0.9	0.05	0.01
SMC [$\mathrm{m^3\,m^{-3}}$]	0.01, 0.05	0.75	0.1	0.001

time-varying VWC. The VWC is adapted each Sentinel-1 time step by optimizing the VWC value on the match between the SMC retrieval and reference of the previous time step. This is based on the assumptions that the residual between a SMC retrieval and reference is caused by an imperfect VWC value and that the VWC value of the previous time step can be used for the current time step. Two methods were tested, namely: (i) combining the Sentinel-1 observations in the ascending and descending orbits, and (ii) separating the ascending (afternoon) and descending (morning) orbits, i.e. using for a descending orbit Sentinel-1 observation the optimum VWC value of the previous descending orbit observation.

2.3. C: Retrieval of soil moisture content from backscatter observations

The retrieval of SMC from a Sentinel-1 σ^0 observation involves finding the SMC value for which the minimum difference between σ^0 simulations and the Sentinel-1 σ^0 observation is achieved. This would require a large number of TV-IEM simulations over a broad range of incidence angle, LAI, VWC and SMC combinations, which is not feasible in operational settings because of the considerable run time of single TV-IEM simulations. Supplement 1 details the estimation of TV-IEM's and IEM's run times. The models require little random access memory (0.3 GB for TV-IEM). On an Intel Core(TM) i7-4790 CPU @ 3.60 GHz processor, the run time is 26.1 s per TV-IEM simulation.

As an alternative, we performed the TV-IEM simulations and stored the σ^0 contributions (σ_v^0, σ_s^0, σ_{sv}^0 and γ^2) in look-up tables. The TV-IEM simulations were first executed on the ranges and coarse simulation increments listed in Table 2. Second, similar to Kim et al. (2014), the TV-IEM simulations were linearly interpolated to the finer increments that are listed in Table 2. This two-step procedure increases the number of nodes from a limited number of simulations, i.e. from 11 880 simulations to 278 633 043 nodes. The validity of the linear interpolations is discussed in Section 3.

To limit the number of TV-IEM simulations, we only performed them for a study region's average soil texture and at discrete incidence angles. IEM's short run time (0.0556 ms per simulation, see Supplement 1) allows to combine the TV-IEM σ_v^0, σ_{sv}^0 and γ^2 simulations, during the retrieval process, with IEM σ_s^0 simulations for the fine interpolation SMC increments and field-specific soil textures and incidence angles.

3. TV-IEM model sensitivity to soil and vegetation variables

The σ_v^0, $\gamma^2\sigma_s^0$ and σ_{sv}^0 relative contributions to the total σ^0, as simulated with the TV-IEM model, are shown in Fig. 3. The fine grid simulated contributions, as functions of LAI and VWC, show small

random deviations from the coarse grid simulations. As a function of SMC, the coarse grid simulations align with the fine grid simulations — for the 35° case — because the coarse grid simulations were combined with IEM simulations at fine increments. However, in contrast with the LAI and VWC, interpolating the simulations for the coarse incidence angle increments to the fine interpolation increments has a systematic effect on the simulations, as can be seen from the systematic deviations in Figs. 3b, d and f. Nevertheless, the linear interpolations of the coarse grid simulations approximately follow the lines of fine grid simulations and in this study we consider the linear interpolations as acceptable approximations for establishing the σ^0 contributions look-up tables.

Figs. 3a–b show that the σ^0 originates completely from the soil surface for a LAI of $0\,\mathrm{m^2\,m^{-2}}$, which is expected because the σ_v^0 and σ_{sv}^0 will be $0\,\mathrm{m^2\,m^{-2}}$ and γ^2 will be 1 when no vegetation is present. However, the $\gamma^2\sigma_s^0$ contribution already reduces significantly with a limited grass cover. The σ_v^0 is larger than the $\gamma^2\sigma_s^0$ from a LAI of approximately $1.5\,\mathrm{m^2\,m^{-2}}$ and onwards (for a VWC of $0.6\,\mathrm{kg\,kg^{-1}}$). Figs. 3c–d show that the $\gamma^2\sigma_s^0$ contribution also reduces with increasing VWC. Hence, both an increasing LAI and VWC cause a diminishing σ^0 to SMC sensitivity. Figs. 3e–f show that the relative $\gamma^2\sigma_s^0$ contribution is larger for higher SMC. This is because σ_s^0 increases with increasing SMC. The σ^0 to SMC sensitivity diminishes with increasing SMC (Altese et al., 1996; Benninga et al., 2019), as is illustrated in Fig. 4. Fig. 4 also reflects the reduced σ^0 to SMC sensitivity under a vegetation cover: the higher the LAI and VWC are, the more the σ^0 to SMC sensitivity reduces because the σ_s^0 is increasingly more attenuated and the σ_v^0 relative contribution to the total σ^0 increases. The $\gamma^2\sigma_s^0$ relative contribution is slightly smaller for the 44° incidence angle than for the 35° incidence angle. This is explained by the longer path through the vegetation for larger incidence angles. For example, for a LAI of $2\,\mathrm{m^2\,m^{-2}}$ and a VWC of $0.6\,\mathrm{kg\,kg^{-1}}$ the γ^2 values are 0.49 and 0.48 for incidence angles of 35° and 44°, respectively, and for a LAI of $4\,\mathrm{m^2\,m^{-2}}$ they are 0.23 and 0.22.

The σ_{sv}^0 relative contribution is small for all grass cover and SMC conditions. The mean σ_{sv}^0 values are 5.5 % of the total σ^0 for the 35° incidence angle (Figs. 3a, c and e) and 3.6 % for the 44° incidence angle (Figs. 3b, d and f). In contrast to the $\gamma^2\sigma_s^0$, the σ_{sv}^0 relative contribution is fairly independent of the LAI and VWC, and under dense grass conditions its contribution is similar to that of the $\gamma^2\sigma_s^0$. Whereas in the frequently-used water cloud model (WCM), which was introduced by Attema and Ulaby (1978) and used in e.g. El Hajj et al. (2017), Paloscia et al. (2013) and Pulvirenti et al. (2018) for SMC mapping from Sentinel-1 imagery, multiple scattering interactions between the soil surface and the vegetation are neglected, these results suggest that σ_{sv}^0 should be included because of its significant contribution to the total σ^0 for grass-covered soil surfaces. Furthermore, σ_{sv}^0 may still contribute to σ^0 to SMC sensitivity under dense vegetation conditions (Chiu and Sarabandi, 2000; Joseph et al., 2010; Stiles et al., 2000).
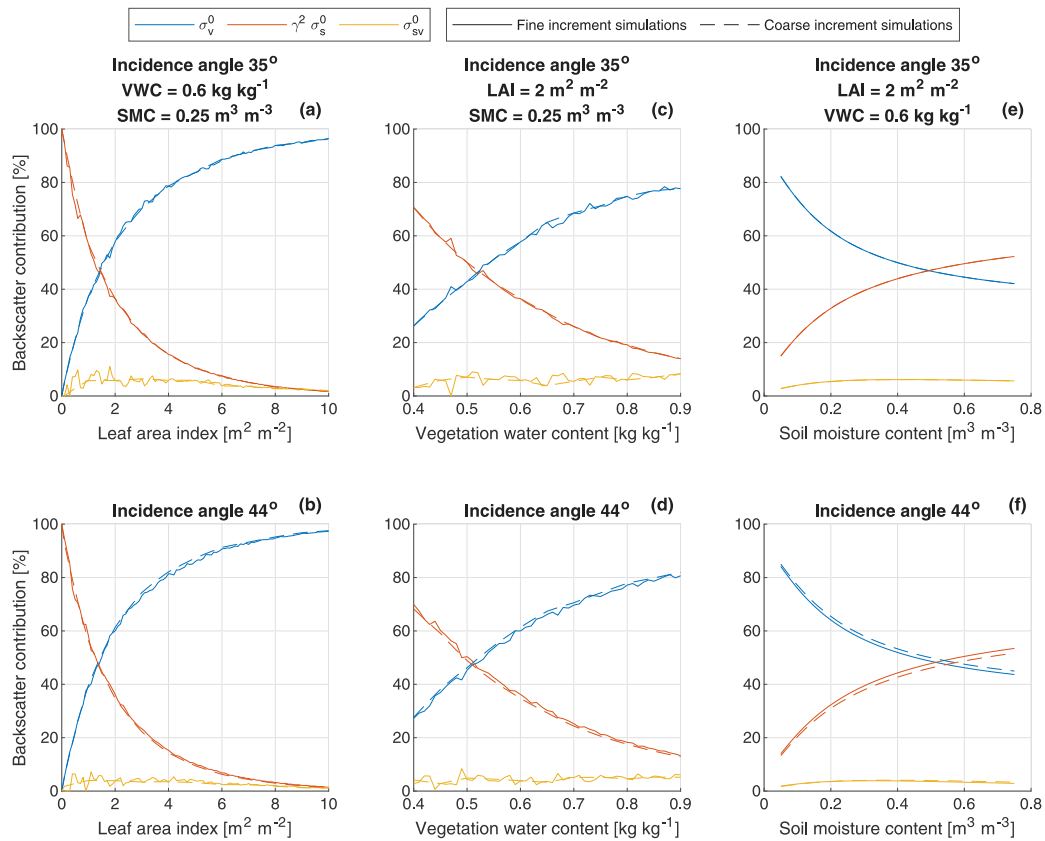
Fig. 3. The σ_v^0, $\gamma^2\sigma_s^0$ and σ_{sv}^0 relative contributions for varied LAI, VWC and SMC conditions, and incidence angles of 35° and 44°. The solid lines represent TV-IEM simulations with fine increments of $0.1\,\mathrm{m^2\,m^{-2}}$ **(a–b)**, $0.01\,\mathrm{kg\,kg^{-1}}$ **(c–d)** and $0.01\,\mathrm{m^3\,m^{-3}}$ **(e–f)**, and the dashed lines represent simulations with the coarse increments listed in Table 2.
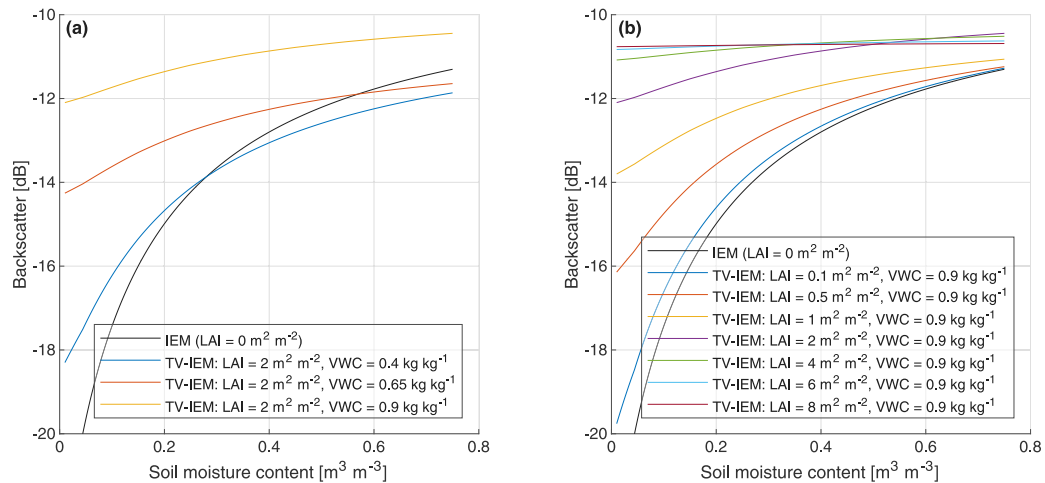

Fig. 4. The sensitivity of σ^0 to SMC. The simulations in this figure are for a 35° incidence angle.

4. Validation references and method

4.1. Study region and period

The study region is located in the eastern part of the Netherlands (Fig. 5a). For an extensive description of the study region's landscape, soils and climate, we refer to Van der Velde et al. (submitted for publication). The region is flat with some elevated glacial ridges (Fig. 5b). From mid-November to mid-March (winter period) the SMC is generally at a high level and from mid-May to mid-October (summer period) at a low level mainly due to a higher evaporative demand (Benninga et al., 2019; Van der Velde et al., 2021). Moreover, the general SMC cycle

contains dynamics on shorter time-scales in response to meteorological events. In the study period of 25 November 2015 to 1 November 2018, the 2018 summer was exceptionally dry due to high evaporative demands and low rainfall (Bakke et al., 2020; Buitink et al., 2020; Buras et al., 2020). The grass growing season is approximately from 1 March to 1 November (Pellikaan, 2017; Veeneman et al., 2017). Outside the growing season, grass covers are virtually static and sparse. Within the growing season meadows are being grazed or cut at several moments, which is why the LAI can be very different between adjacent meadows (see Fig. 2).
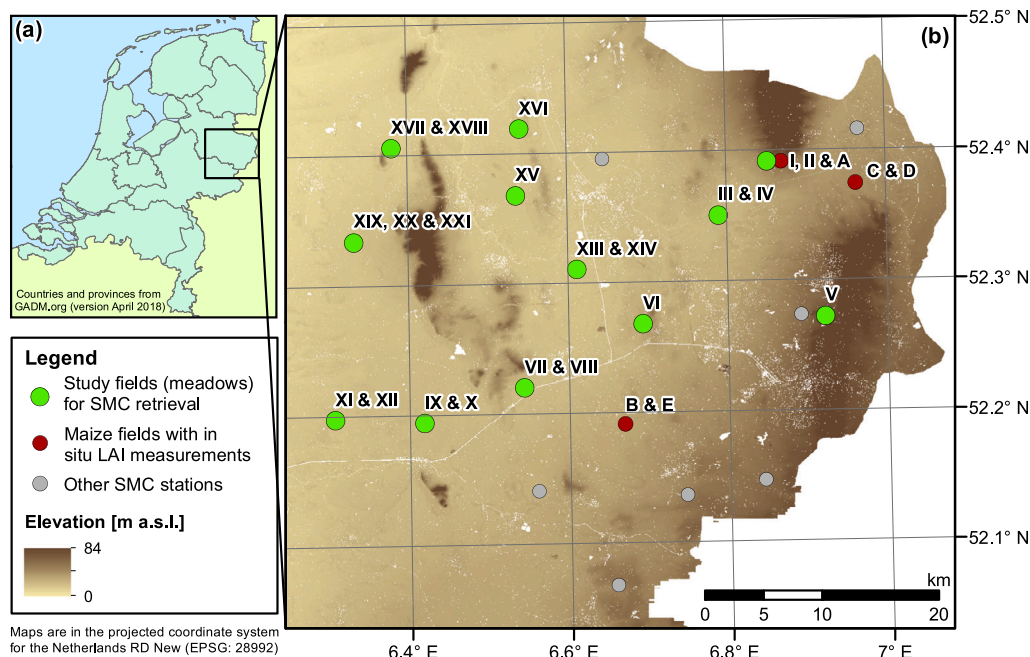
Fig. 5. **(a)** Location of the study region in the Netherlands. **(b)** The locations of the study fields, adjacent to stations of the SMC monitoring network Twente (Dente et al., 2012, 2011; Van der Velde et al., submitted for publication; Van der Velde and Benninga, 2022). Background is the digital terrain model AHN2 (Actueel Hoogtebestand Nederland, 2012).

Table 3

Specifications of the Sentinel-1 orbits that cover the study region. CET stands for Central European Time. The number of Sentinel-1 images is for the study period from 25 November 2015 to 1 November 2018 and before masking the σ^0 observations for weather-related surface conditions.

Relative orbit number	Pass	Acquisition time (CET)	Number of Sentinel-1 images	Projected local incidence angle over the study fields
15	Ascending	18:16	145	32.3° to 36.3°
37	Descending	6:49	148	34.0° to 37.8°
88	Ascending	18:24	143	40.8° to 44.4°
139	Descending	6:41	146	42.2° to 45.6°

The imaging revisit time of the Sentinel-1 satellites over a region is controlled by a region's latitude and Sentinel-1's acquisition strategy (Bauer-Marschallinger et al., 2019; Torres et al., 2012). Sentinel-1 images are collected relatively intensively over our study region because this region is covered by two ascending and two descending orbits. The characteristics of these orbits are listed in Table 3. Sentinel-1's imaging revisit time over the study region with these four orbits combined and both Sentinel-1A and -1B is 1.5 days. The Sentinel-2 LAI maps were available for specific time periods and specific parts of Europe (Paepen and Wens, 2017; VITO, 2019): for the northern part of our study region throughout the study period, but for the southern part the period from 1 January 2017 to 1 July 2018 was not available and for the most eastern part only half of the Sentinel-2 images were processed. This gives temporal resolutions of 4 days for the western and middle part and 8 days for the eastern part of the study region.

4.1.1. In situ soil moisture content

The study region is equipped with a network of twenty SMC monitoring stations, known as the Twente network (Dente et al., 2012, 2011; Van der Velde et al., submitted for publication; Van der Velde and Benninga, 2022) and shown in Fig. 5b. The retrieval scheme was applied to estimate SMC for the meadows adjacent to monitoring stations. Multiple meadows can be adjacent to a single SMC station, as can also be seen in Fig. 2. Table S2 (in supplementary material) lists the study fields with their surface areas and number of Sentinel-1 pixels. The study fields' surface areas (number of pixels) range from 0.16 ha (24 pixels) to 6.3 ha (1026 pixels). Sentinel-1's radiometric

uncertainty reduces with the surface area over which σ^0 observations are averaged (Benninga et al., 2019), so it can be expected that the respective SMC retrieval performance depends on the surface area of a study field. Investigating the effect of a field's surface area on SMC retrieval performance is, however, outside the scope of this paper.

Table S2 also lists the soil characteristics of the study fields. Sandy to loamy sandy soils dominate the surface layer in the study region, with some remnants of loamy soils and organic soils (Van der Velde et al., submitted for publication; Wösten et al., 2013). This study was limited to the meadows with sandy to loamy sandy surface layers. We generated TV look-up tables for the study fields' average soil texture of 80 % sand, 15 % silt and 5 % clay, with a bulk density of $1.33\,\mathrm{g\,cm^{-3}}$, derived from BOFEK2012 (Wösten et al., 2013). As explained in Section 2.3, IEM was run for the field-specific soil textures.

The monitoring stations measure SMC with 5TM probes (METER Group, 2019) at nominal depths of 5 cm, 10 cm, 20 cm, 40 cm and 80 cm and store the readings every 15 min. The 5TM probes have an influence zone of approximately up to 4 cm above and below the sensor's middle prong (Benninga et al., 2018). We used the 5 cm depth SMC measurements, being representative for a soil depth of 1 cm to 9 cm, that are collected at Sentinel-1 overpass times as the in situ references. The in situ SMC measurements that were impacted by frozen soil conditions (Van der Velde et al., 2021) were discarded as references. Furthermore, Benninga et al. (2020) reported that the SMC time series from Twente monitoring stations capture the temporal dynamics but the absolute values exceed realistic ranges for SMC. To validate the temporal dynamics, we applied the bias correction procedure that is explained in Section 4.2.

Two uncertainties of the references are the sensors' measurement uncertainty (Cosh et al., 2005) and a spatial mismatch uncertainty (Cosh et al., 2006; Western et al., 2002). Van der Velde et al. (submitted for publication) describes the calibration of the 5TM probes on the Twente region's soils. The measurement uncertainty, quantified against gravimetrically determined volumetric SMC with the root mean square deviation ($RMSD$), is $0.028\,\mathrm{m^3\,m^{-3}}$. Horizontal and vertical mismatch uncertainties exist between the SMC references and Sentinel-1 observed SMC (Benninga et al., 2020; Benninga, 2022). For the horizontal and vertical mismatch uncertainties together, i.e. the spatial mismatch uncertainty, a common estimate of $0.051\,\mathrm{m^3\,m^{-3}}$ was found. Benninga et al. (2020) demonstrated that the references' sensor uncertainty and spatial mismatch uncertainty constitute, respectively, 13 % and 46 % of the retrieval uncertainty at a SMC of $0.26\,\mathrm{m^3\,m^{-3}}$ to 4 % and 15 % at a SMC of $0.53\,\mathrm{m^3\,m^{-3}}$; i.e., these are major uncertainty contributions in the evaluation of satellite SMC retrievals.

4.1.2. In situ leaf area index

The interpolated Sentinel-2 LAI estimates were validated against in situ references. During the growing seasons of 2016 and 2017, we measured the LAI on two meadows (fields I and III) on a two-weekly basis. In order to increase the number of available LAI references and evaluate the general performance of the Sentinel-2 LAI estimates, we also validated them with in situ LAI measurements that were collected on four maize fields (fields A–D). In situ LAI measurements were also collected on a fifth maize field (field E), but no concurrent Sentinel-2 LAI estimates are available here.

Fig. 5b shows the locations of fields I, III and A–E, and Fig. 2 shows the locations of the LAI measurements within these fields. The LAI measurements were collected at three to six locations, about 50 m to 100 m apart, within a field. The optical instrument LI-COR LAI-2000 (LI-COR, 1992) was used for the measurements. This instrument estimates the LAI based on the ratio between light intensity readings above and below the canopy. We operated the instrument with a sensor opening of 90° to remove the operator and the sun from the sensor's view (LI-COR, 1992). On the meadows we acquired one above-canopy reading and four below-canopy readings about 0.5 m apart to reduce the measurement uncertainty. On the maize fields we acquired, at each measurement location, four below-canopy readings with the sensor opening along the rows and four below-canopy readings with the sensor opening facing a maize row, each set accompanied with an above-canopy reading. Of the four measurements below a maize canopy, the first was in/adjacent to the maize row, the second was at 1/4 between rows, the third was halfway, and the fourth was at 3/4 between rows, following the LAI-2000 manual (LI-COR, 1992). The LAI-2000 File Viewer (FV2000) application (LI-COR, 2004), using the default horizontal uniform canopy model, converted the light intensity readings to LAI.

The Sentinel-2 LAI estimates and the in situ references are shown in Fig. 6. Following the conditions for the interpolation of Sentinel-2 LAI estimates as defined in Section 2.1.2, during harvesting periods the Sentinel-2 LAI estimates are indeed not interpolated. As a result, however, no validation pair is established for the in situ LAI references that were acquired just before or after a harvesting period. These in situ LAI references typically represent the most extreme LAI conditions. As the LAI will not vary much in the week before and the week after harvesting, we relaxed the maximum time gap of 1.5 days to maximum one week for these LAI references and included them as pairs with the Sentinel-2 LAI estimate just before or after.

4.2. CDF matching

Discrepancies between retrievals and references are present due to errors in both data sets, as well as due to spatial scale and depth mismatches (Kornelsen and Coulibaly, 2015; Drusch et al., 2005; Draper et al., 2009; Wagner et al., 2007). Such discrepancies appear as biases

in the mean, variability, dynamic range and more (Drusch et al., 2005; Reichle and Koster, 2004), and hinder meaningful validation of absolute values (Draper et al., 2009; Wagner et al., 2007; Kornelsen and Coulibaly, 2015; Brocca et al., 2011). Examples are those SMC values from Twente monitoring stations exceeding realistic ranges as noted in Section 4.1.1. Besides, assimilating a satellite SMC product into a land surface model or combining multiple satellite SMC products would require that their statistical moments match (Drusch et al., 2005; Reichle and Koster, 2004). Kornelsen and Coulibaly (2015) and Draper et al. (2009) stated that the main use of SMC retrievals from satellite observations is to represent the temporal dynamics, and bias correction is an important step in isolating and validating this.

Cumulative distribution function (CDF) matching effectively suppresses systematic biases in the mean, variability and dynamic range of estimates — e.g. the Sentinel-1 SMC retrievals — with their respective references (Boé et al., 2007; Brocca et al., 2011; Drusch et al., 2005; Kornelsen and Coulibaly, 2015; Reichle and Koster, 2004). CDF matching was implemented by fitting a polynomial (correction function) to ranked retrievals against the residuals between the ranked retrievals and ranked references (Brocca et al., 2011; Drusch et al., 2005; Kornelsen and Coulibaly, 2015). The correction function is generated on retrieval–reference pairs. We obtained the model coefficients of the correction function with the 'Trust-Region' algorithm in Matlab's Curve Fitting toolbox, by fitting, similar to Brocca et al. (2011), a fifth-order polynomial.

After generation of the correction function, the Sentinel-1 SMC retrievals were subjected to the correction function so that their CDF should match the in situ SMC references' CDF. The Kolmogorov–Smirnov test with a significance level of 5 % (Kornelsen and Coulibaly, 2015; Massey, 1951) was used to verify whether the correction function successfully aligned the CDFs. If this is confirmed, the correction function was also applied to the retrievals for which no concurrent reference is available and beyond the range for which it was developed. Following Boé et al. (2007), the correction factor of the correction function's boundary was applied to retrievals that exceed the ranges on which the correction function was established.

4.3. Performance metrics

The Sentinel-2 LAI estimates and Sentinel-1 SMC retrievals were evaluated against their in situ references with the Pearson correlation coefficient (r_P), the root mean square deviation ($RMSD$) and the unbiased $RMSD$ ($uRMSD$), which are defined as follows:

$$r_P = \frac{\sum_{t=1}^{N} \left(Y_e(t) - \overline{Y_e} \right)\left(Y_r(t) - \overline{Y_r} \right)}{\sqrt{\sum_{t=1}^{N} \left(Y_e(t) - \overline{Y_e} \right)^2}\sqrt{\sum_{t=1}^{N} \left(Y_r(t) - \overline{Y_r} \right)^2}}, \tag{2}$$

$$RMSD = \sqrt{\frac{\sum_{t=1}^{N} \left(Y_e(t) - Y_r(t) \right)^2}{N}}, \tag{3}$$

and

$$uRMSD = \sqrt{\frac{\sum_{t=1}^{N} \left(Y_e(t) + \left(\overline{Y_r} - \overline{Y_e} \right) - Y_r(t) \right)^2}{N}}, \tag{4}$$

where N stands for the number of pairs, Y_e and Y_r for the estimates and the references, respectively, t for the observation number and the bars for the means of Y_e and Y_r. The $uRMSD$ was not reported for the SMC retrievals because CDF matching removes systematic biases between the means of SMC retrievals and references, resulting in equal $RMSD$ and $uRMSD$. The $uRMSD$, or $RMSD$ for the SMC retrievals,
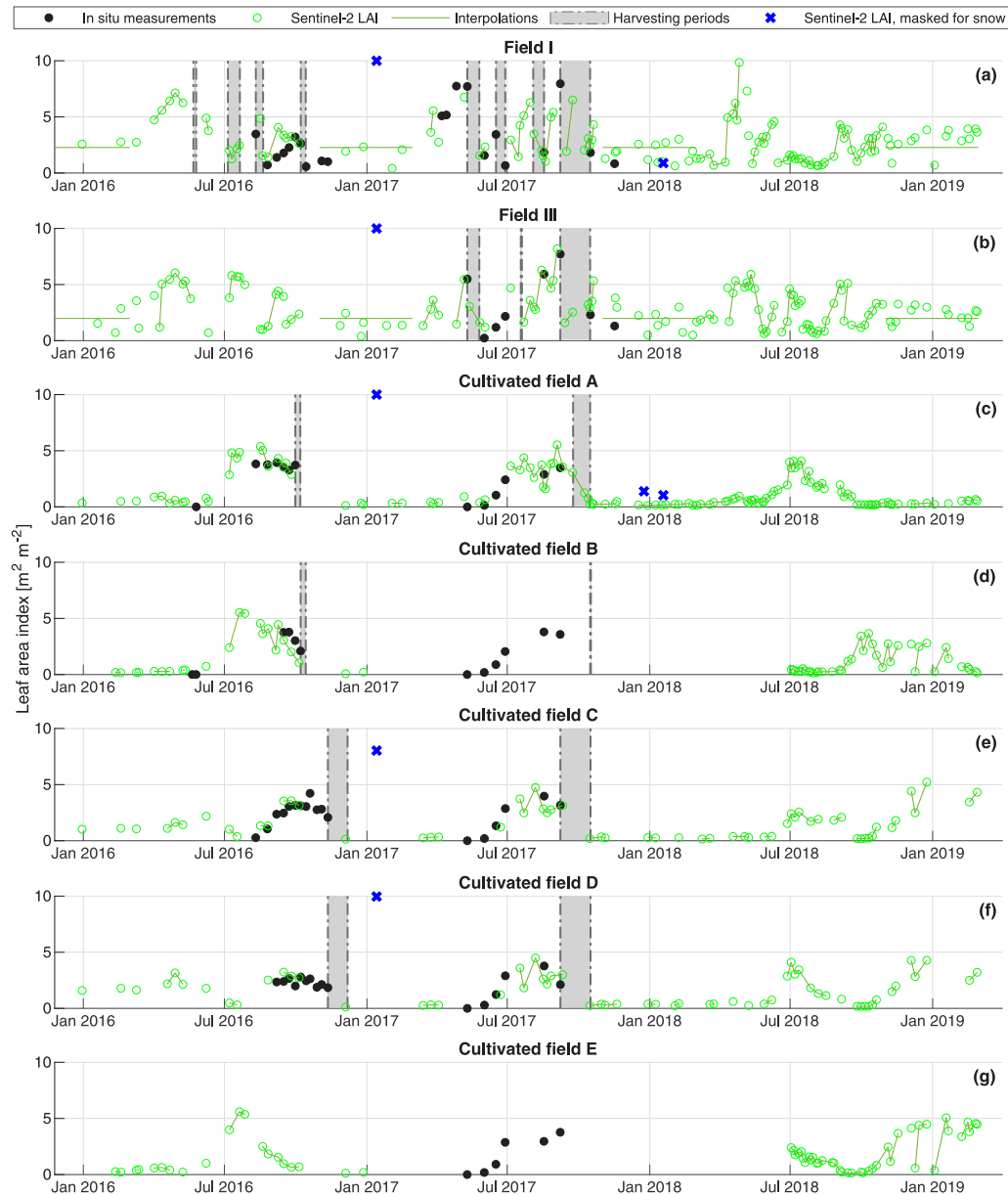
Fig. 6. Sentinel-2 LAI estimates and in situ LAI references.

is the standard deviation of the differences between estimates and references (Kerr et al., 2016), and can, as such, be considered as a measure of uncertainty.

The r_P and the relative $RMSD$ ($RRMSD$) were used for comparison of the SMC retrieval performance among fields and against the performance of other SMC products. The $RRMSD$ is defined as follows:

$$RRMSD = \frac{RMSD}{\max(Y_r) - \min(Y_r)}, \qquad (5)$$

where $\max(Y_r)$ and $\min(Y_r)$ stand for the maximum and minimum Y_r. The $RRMSD$ evaluates the retrieval uncertainty relative to the range of the SMC references. In contrast to the $RMSD$, of which the value depends on the range of SMC values that occur, the $RRMSD$ may be compared among fields, conditions or studies with different SMC ranges. We calculated the $RRMSD$ of other studies using the reported unbiased $RMSD$ values and SMC ranges or, if available, the original SMC retrievals and references.

5. Results and discussion

5.1. Sentinel-2 leaf area index

5.1.1. Validation

The time series of the Sentinel-2 LAI estimates and the in situ LAI references in Fig. 6 show the same dynamics. The Sentinel-2 LAI product, thus, provides information of vegetation conditions at field scale. Table 4 lists the performance metrics between the linearly interpolated Sentinel-2 LAI estimates and the in situ references. However, the Sentinel-2 LAI estimates that were acquired when snow was present seem disturbed. Therefore, in addition to the default masking for cloud shadow, medium probability for clouds and high probability for clouds, we also masked the Sentinel-2 LAI maps when the scene classification of snow applies to a pixel. For the maize fields no in situ references are available in winter, but for the meadows the performance metrics (see Table 4) indeed slightly improve. The match between the final Sentinel-2 LAI estimates and the in situ references is presented in Fig. 7.

Table 4
Performance metrics of two Sentinel-2 LAI products against the in situ references collected on the meadows and maize fields.

Study fields	LAI product	Number of pairs	r_P [–]	$RMSD$ [m^2 m^{-2}]	$uRMSD$ [m^2 m^{-2}]
Meadows	Original	21	0.93	1.15	0.84
	Masked for snow	21	0.93	1.11	0.82
Maize	Original	23	0.63	0.83	0.82
	Masked for snow	23	0.63	0.83	0.82
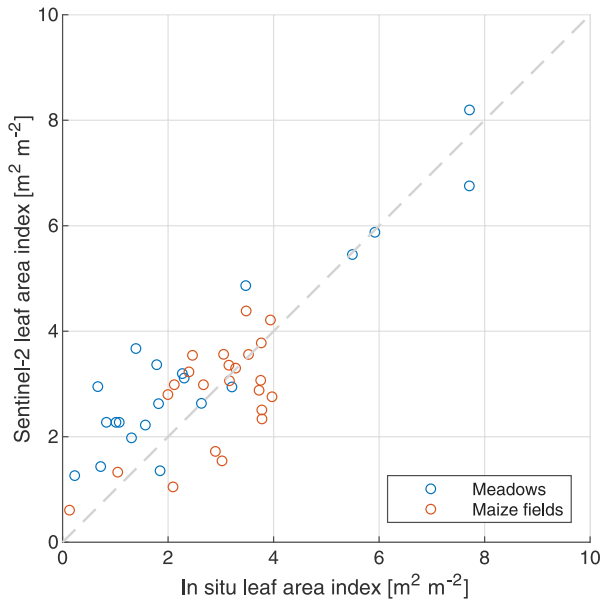
Fig. 7. The Sentinel-2 LAI estimates, after masking for snow, against the in situ LAI references collected on the meadows and maize fields.

The uncertainty of the linearly interpolated Sentinel-2 LAI estimates for the meadows is estimated at 0.82 m^2 m^{-2}.

5.1.2. Propagation of Sentinel-2 leaf area index uncertainty

The uncertainty of the Sentinel-2 LAI estimates propagates through the TV-IEM SMC retrieval scheme and affects SMC retrievals. We investigated this effect by retrieving the SMC from a σ^0 value for a given LAI value as well as for this LAI value perturbed upwards and downwards with the Sentinel-2 LAI uncertainty of 0.82 m^2 m^{-2}. This propagation principle can be deduced from Fig. 4b and is illustrated in more detail in Supplement 3.

Fig. 8 shows the effect of the Sentinel-2 LAI uncertainty on the SMC retrievals. The σ^0 to SMC relation is more sensitive to the LAI in the lower LAI range, e.g. a LAI of 2 m^2 m^{-2}, as is reflected in Fig. 4b. This causes in many cases even invalid SMC retrievals above or below the retrieval limit. In the upper range of LAI values the σ^0 to SMC sensitivity diminishes, causing that a same deviation in σ^0 results in a larger deviation in SMC.

5.2. Calibration of the vegetation water content

Fig. 9 shows the performance of SMC retrievals for a range of time-invariant VWC values and the time-varying methods, as explained in Section 2.2.2. Both the r_P and $RMSD$ are hardly affected by the used VWC. This suggests that other uncertainties, such as the Sentinel-1 radiometric uncertainty (see Section 2.1.1), surface roughness parameter uncertainty (Benninga et al., 2020), SMC references' uncertainties (see Section 4.1.1) and Sentinel-2 LAI uncertainty (Section 5.1.2), dominate the retrieval uncertainty. Moreover, temporal variation in the vegetation status is included via the LAI time series: when the VWC is

low, the LAI will also tend to be lower. This is illustrated in Fig. 6a–b for example for the very dry 2018 summer and this reduces the sensitivity of the model performance to VWC.

The highest r_P and lowest $RMSD$ are obtained for a VWC of 0.90 kg kg^{-1}. This value also outperforms the two time-varying VWC methods. In addition, the time-varying VWC methods have the disadvantage of requiring a SMC reference for the previous Sentinel-1 time step, which will generally not be available in operational applications. Therefore, the VWC value of 0.90 kg kg^{-1} was selected as input to the SMC retrieval scheme.

5.3. Soil moisture content retrievals

Fig. 10 shows time series and CDFs of SMC retrievals and references for field XVIII, XIV and II, respectively the fields with the best, worst and a medium $RRMSD$ performance. The CDF matching is successful in aligning the SMC retrievals' CDFs to the references' CDFs. All fields pass the Kolmogorov–Smirnov test with a significance level of 5 % (Kornelsen and Coulibaly, 2015; Massey, 1951). The time series in the left panels demonstrate that the retrievals match the SMC references pretty well, although the retrievals also exhibit a significant spread, i.e. uncertainty, and there are periods with systematic deviations from the references.

As a result of the successful CDF matching, over the complete period no systematic differences between the IEM and TV-IEM SMC retrievals are present. Nevertheless, their retrievals are different due to the different pairs that were used in the CDF matching and due to the vegetation correction. The vegetation correction (without considering the CDF matching) causes that the majority of the vegetation-corrected TV-IEM retrievals is lower than the IEM retrievals. For most combinations of LAI, VWC and SMC, the vegetation contributes more to the σ_v^0 and σ_{sv}^0 than that it attenuates the σ_s^0. This is shown in Fig. 4b by the higher SMC-σ^0 lines with vegetation present.

5.3.1. The performance of IEM and TV-IEM retrievals

Fig. 11 shows the performance metrics of the SMC retrievals. More SMC retrievals are possible if no vegetation correction is applied because not for every Sentinel-1 σ^0 observation a Sentinel-2 LAI estimate is available and because TV-IEM results in more invalid SMC retrievals above or below the retrieval limit. Averaged over the study fields, there are 164.9 and 322.9 SMC retrievals possible for the total period and 103.4 and 261.4 for the growing seasons with TV-IEM and IEM respectively. The performance metrics of the IEM retrievals for the same retrieval–reference pairs as TV-IEM are also shown in Fig. 11.

The performance metrics of the SMC retrievals with TV-IEM are slightly better than the performance metrics of 'IEM all retrievals', especially regarding r_P. Comparison with the performance metrics of IEM shows, however, that this effect is caused by the different retrieval–references pairs. The invalid TV-IEM retrievals occur mainly under denser vegetation conditions because the range of σ^0 values for which a SMC retrieval is possible becomes limited, as can be seen in Fig. 4b. When a Sentinel-1 σ^0 observation is outside this range, the SMC retrieval will be invalid. Under denser vegetation cover, i.e. increasing LAI, the σ^0 to SMC sensitivity reduces (see Section 3). IEM does not account for the effect of vegetation, as a result of which the Sentinel-1 σ^0 observations that led to the invalid SMC retrievals by TV-IEM yield less accurate SMC retrievals by IEM under the denser vegetation conditions and negatively impact the performance metrics.

Although it could be expected that correcting σ^0 observations for vegetation effects contributes to better SMC retrieval performances, the similar performance metrics for TV-IEM and IEM may be explained by two factors. Firstly, Section 5.1.2 demonstrates the substantial effect of the Sentinel-2 LAI uncertainty on SMC retrievals. It is likely that the correction required for grass is dominated by the uncertainty that is introduced by the Sentinel-2 LAI estimates. Secondly, the effect of grass on the Sentinel-1 σ^0 may be not as large as simulated with the
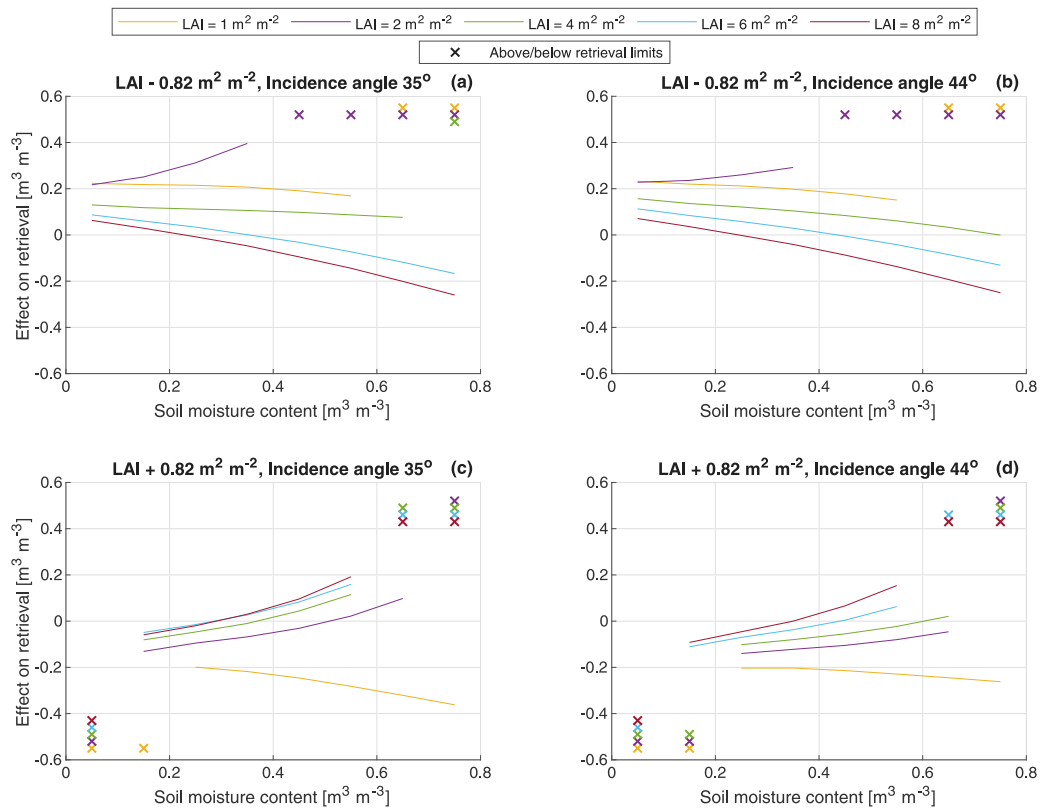
Fig. 8. The propagation of the Sentinel-2 LAI uncertainty ($0.82\,\text{m}^2\,\text{m}^{-2}$) into TV-IEM SMC retrievals. The SMC retrievals limits are $0.01\,\text{m}^3\,\text{m}^{-3}$ and $0.75\,\text{m}^3\,\text{m}^{-3}$. Exceedances of these limits after perturbation of the LAI are shown as crosses. These figures are for a VWC of $0.90\,\text{kg}\,\text{kg}^{-1}$, which followed from its calibration (Section 5.2).
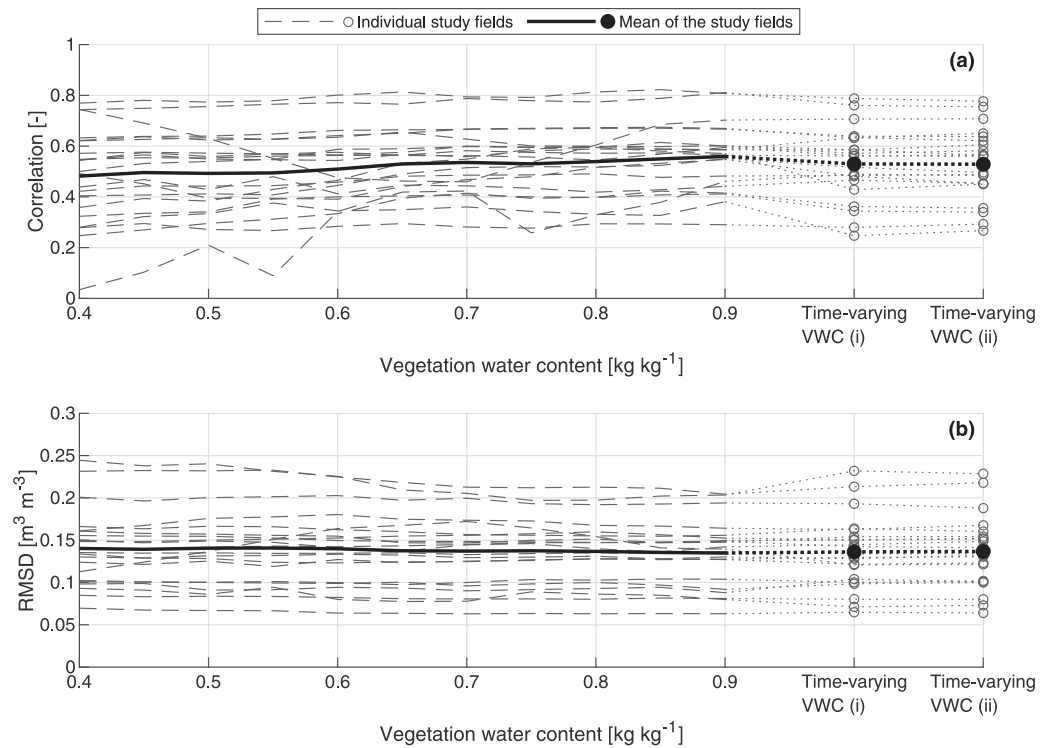

Fig. 9. Performance metrics between SMC retrievals and references for a range of time-invariant VWC values and the time-varying VWC methods (i) and (ii).

TV model, which would cause incorrect corrections for the vegetation effects. This is supported by the results in Benninga et al. (2020),

in which it was found that the uncertainty of SMC retrievals can be explained even when the vegetation effects are not considered. The
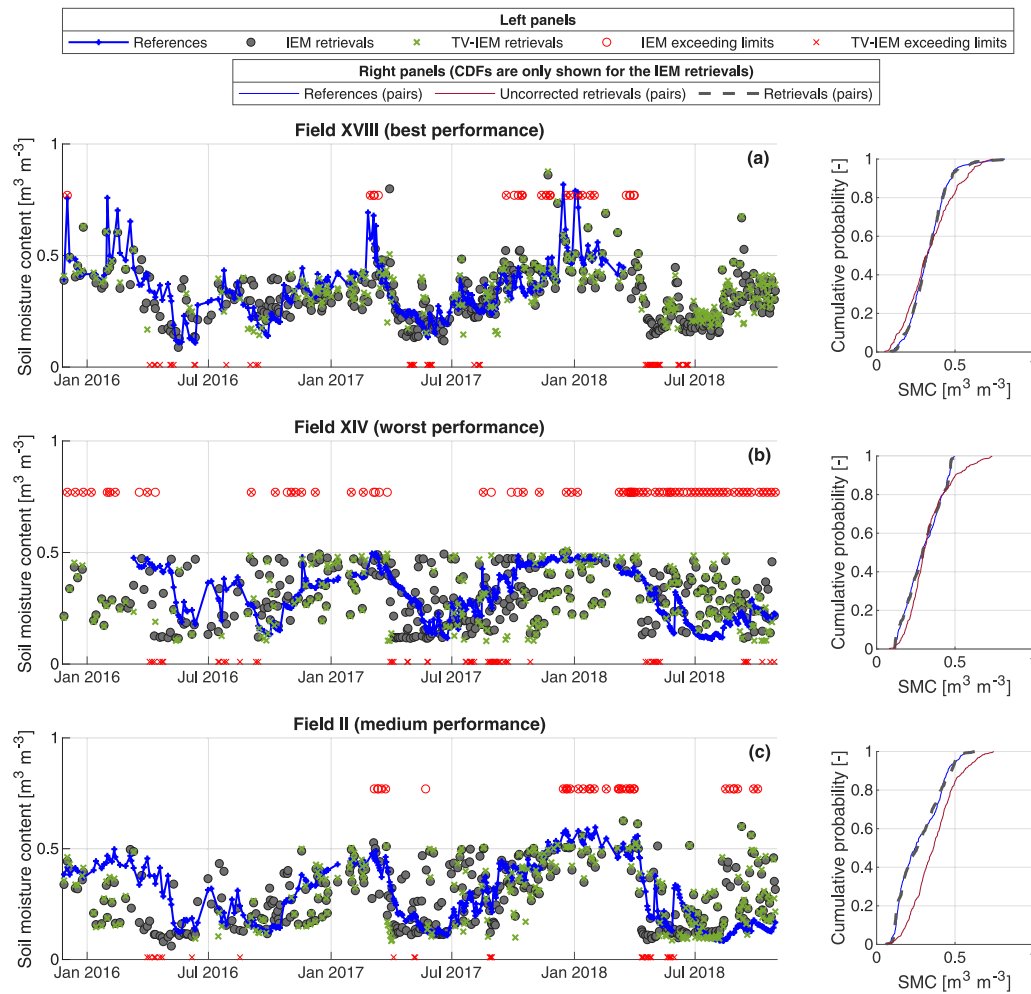
Fig. 10. SMC retrievals and references for field XVIII (best retrieval performance), field XIV (worst performance) and field II (medium performance). The CDFs (right panels) are only shown for the IEM retrievals. (For interpretation of the references to colour in this figure legend, the reader is referred to the web version of this article.)

LAIs of the meadows in that study were $1.1\,\text{m}^2\,\text{m}^{-2}$ and $1.3\,\text{m}^2\,\text{m}^{-2}$, and their results suggest that the vegetation effects could be neglected under these sparse vegetation conditions. Similar results were found by Van der Velde et al. (2012) and Van der Velde and Su (2009). In contrast, the vegetation effects as simulated by the TV model are significant at LAI values of $1.1\,\text{m}^2\,\text{m}^{-2}$ and $1.3\,\text{m}^2\,\text{m}^{-2}$, with, for a 35° incidence angle, γ^2 values of 0.50 and 0.45 and σ_v^0 values of $-14.0\,\text{dB}$ and $-13.6\,\text{dB}$ respectively. Considering the vegetation parameters, which in this paper were adopted from a calibration on an alpine meadow landscape, may be a way for improving the vegetation correction model and the TV-IEM SMC retrievals.

5.3.2. Exceedance of retrieval limits

One result we want to highlight is obtained for field XXI (Fig. 12): hardly any Sentinel-1 σ^0 observation resulted in a valid SMC retrieval between 25 November 2015 and 26 March 2017. The crop parcel registry (Ministry of Economic Affairs and Climate Policy, 2020) lists that this field was used to grow maize in 2015 and 2016, and only since 2017 it has been in use as meadow. Fig. 12 shows that this has a large effect on the SMC retrievals and results in many invalid retrievals, i.e. the Sentinel-1 σ^0 observation does not correspond to a SMC between $0.01\,\text{m}^3\,\text{m}^{-3}$ and $0.75\,\text{m}^3\,\text{m}^{-3}$ according to the modelled σ^0 to SMC relation. This can be explained by the surface roughness that is different for maize fields than for meadows (Benninga et al., 2020). In all performance results, therefore, only the period after 26 March 2017 was evaluated for field XXI. For the other fields, valid SMC retrievals are found throughout the study period. The used surface roughness

parameters, thus, provide a reasonable representation of the surface roughness for the meadows.

SMC retrievals for the other fields exceed the upper retrieval limit of $0.75\,\text{m}^3\,\text{m}^{-3}$ mainly in wet periods, and this may, as such, provide information about the SMC. To test this, we set the retrievals that exceed $0.75\,\text{m}^3\,\text{m}^{-3}$ to the maximum SMC. For example, for field II these retrievals (red data points in Fig. 10c) were set to $0.63\,\text{m}^3\,\text{m}^{-3}$. This was applied to all the SMC retrievals exceeding the upper limit (variant 1) and only to those retrievals in the period from 15 November to 15 March (variant 2), which is the expected wet period in the study region. As shown in Figs. S4–S5 and summarized in Table 5, both variants improve the r_P in particular. Variant 2 results in the best SMC retrieval performance for both IEM and TV-IEM. The σ^0 to SMC sensitivity simulated with IEM diminishes with increasing SMC. However, the σ^0 signal does not completely saturate until $0.75\,\text{m}^3\,\text{m}^{-3}$ (see Fig. 4). This result — of setting the SMC retrievals that exceed the upper retrieval limit to the maximum SMC improving the SMC retrieval performances — confirms that the σ^0 signal, under very wet conditions, can still provide information. Setting retrievals that exceed the lower limit of $0.01\,\text{m}^3\,\text{m}^{-3}$ to the minimum SMC was also tested, but this does not improve the IEM and TV-IEM retrieval performances.

5.3.3. Masking for dense vegetation

The SMC retrievals will be less accurate under denser vegetation conditions. El Hajj et al. (2017) acknowledged this limitation of C-band SAR σ^0 observations by masking the σ^0 observations acquired
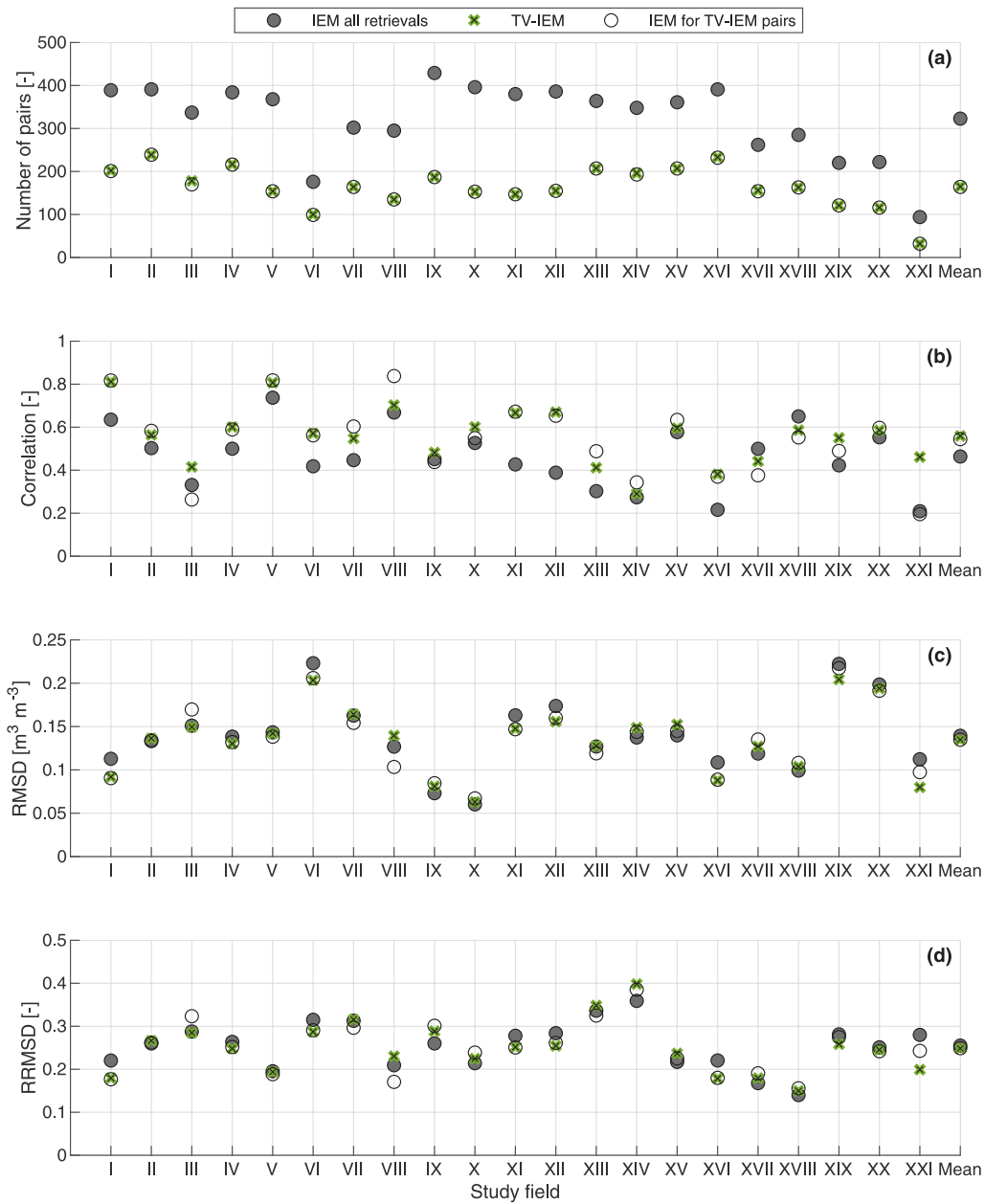
Fig. 11. Performance metrics of the IEM and TV-IEM SMC retrievals against the SMC references. 'IEM for TV-IEM pairs' contains the same retrieval–reference pairs as 'TV-IEM' (i.e. a Sentinel-2 LAI estimate is available and TV-IEM resulted in a valid SMC retrieval), whereas 'IEM all retrievals' contains all the retrieval–reference pairs possible (i.e. from all the Sentinel-1 σ^0 observations).

Table 5

Performance metric means of the study fields for two variants of incorporating information from SMC retrievals that exceed the upper retrieval limit of $0.75\,\mathrm{m^3\,m^{-3}}$. Variant 1 sets all the IEM retrievals that exceed $0.75\,\mathrm{m^3\,m^{-3}}$ and variant 2 sets only the IEM retrievals that exceed $0.75\,\mathrm{m^3\,m^{-3}}$ in the expected wet period (15 November to 15 March) to the maximum SMC. The performance metrics per study field are shown in Figs. S4–S5.

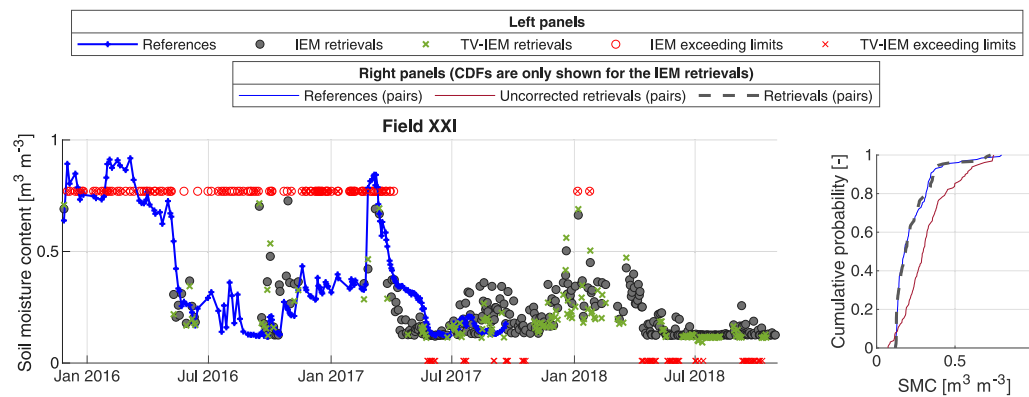| SMC product	Variant	Number of pairs	r_P [–]	$RMSD$ [$\mathrm{m^3\,m^{-3}}$]	$RRMSD$ [–]
	Original	322.9	0.46	0.14	0.25
IEM all retrievals	1	352.2	0.54	0.15	0.25
	2	339.5	0.55	0.14	0.24
	Original	164.9	0.56	0.13	0.25
TV-IEM	1	186.2	0.61	0.14	0.25
	2	179.0	0.64	0.13	0.24
	Original	164.0	0.54	0.13	0.25
IEM for TV-IEM pairs	1	186.2	0.59	0.14	0.25
	2	178.2	0.62	0.13	0.24

Fig. 12. SMC retrievals and references for field XXI. Only since 2017 this field has been in use as meadow, resulting in many invalid retrievals in the period before due to a different surface roughness.

under vegetation conditions with a NDVI higher than 0.75. Applying the relation reported in Knyazikhin et al. (1999) and Tesemma et al. (2014), a NDVI of 0.75 converts into a LAI of $5.63\,\mathrm{m^2\,m^{-2}}$. This might even be a too high LAI threshold, as the σ^0 to SMC sensitivity, according to the TV model (Fig. 4), is already significantly reduced at a LAI of $2\,\mathrm{m^2\,m^{-2}}$.

The performance of the IEM SMC retrievals was analysed for a range of LAI thresholds used to mask the SMC retrievals. For example, for a LAI threshold of $4\,\mathrm{m^2\,m^{-2}}$ we masked all SMC retrievals from Sentinel-1 σ^0 observations that were acquired when the Sentinel-2 LAI estimate was higher than $4\,\mathrm{m^2\,m^{-2}}$. Fig. 13 shows that the performance metrics improve with the LAI threshold. However, the number of pairs also reduces with application of a (lower) LAI threshold. Applying a certain LAI threshold for masking SMC retrievals is, thus, a trade-off between accuracy and number of retrievals.

5.4. Retrieval performance compared with other studies

The SMC retrieval performances were compared with the performances of two other Sentinel-1 based products at field scale (El Hajj et al., 2017; Carranza et al., 2019), one Sentinel-1 and a priori SMC information based product at field scale (El Hajj et al., 2017), three Sentinel-1 based products at $1\,\mathrm{km}$ resolution (Bazzi et al., 2019; Bauer-Marschallinger et al., 2019; Balenzano et al., 2021), and the SMAP $9\,\mathrm{km}$ (Pezij et al., 2020; Chan et al., 2018) and $36\,\mathrm{km}$ products (Van der Velde et al., 2021; Chan et al., 2016) evaluated against single stations. The comparison between performances of products from different studies is obscured by different study region characteristics and qualities of references. An example are the land covers: For the SMAP $9\,\mathrm{km}$ and $36\,\mathrm{km}$ products we selected the SMC monitoring stations in meadow landscapes, as for the retrieval scheme presented in this paper. The products of El Hajj et al. (2017) and Bazzi et al. (2019), Carranza et al. (2019), and Balenzano et al. (2021) were evaluated on study areas used for cultivating approximately half grassland and half wheat, a variety of crops, and mainly wheat, respectively, which have different scattering processes. Nevertheless, the comparison helps valuing the obtained retrieval performances. The product characteristics and performance metrics are listed in Table 6, and discussed in the sections below.

5.4.1. Comparison with Sentinel-1 based products
The performance metrics of the two Sentinel-1 based products at field-scale — the first product in El Hajj et al. (2017) and the product in Carranza et al. (2019) — are similar to the performances we obtained. Note that the SMC retrievals in El Hajj et al. (2017) are compared to references based on 25 to 30 measurements within a study field. The references' sensor measurement uncertainty and spatial mismatch uncertainty are major uncertainty contributions in

the evaluation of satellite SMC retrievals (see Section 4.1.1). These uncertainty contributions are reduced by averaging spatially distributed measurements (Balenzano et al., 2021; Singh et al., 2020; Vinnikov et al., 1999), as in El Hajj et al. (2017). As such, the actual $RRMSD$, which excludes the references' uncertainties, of the SMC products in this study are expected to be lower than that of the product in El Hajj et al. (2017). The second product in El Hajj et al. (2017) has a better SMC retrieval performance than the algorithm presented in this paper, which is explained by the use of a priori information on the SMC condition. The products in Bazzi et al. (2019) and in Balenzano et al. (2021) also show better performance metrics. This can be explained by the lower references' uncertainties and the lower radiometric uncertainty (Benninga et al., 2019) at the $1\,\mathrm{km}$ or $1.6\,\mathrm{km}$ scale than at the field scale of $0.16\,\mathrm{ha}$ to $6.3\,\mathrm{ha}$ that is studied here.

5.4.2. Comparison with SMAP products
The SMAP $36\,\mathrm{km}$ and $9\,\mathrm{km}$ products perform better at field scale than the Sentinel-1-based SMC products in this study and the other studies listed in Table 6. The SMAP imagery — in L-band — are less obstructed by vegetation and more sensitive to SMC as well as have a sampling depth closer to the references at $5\,\mathrm{cm}$ depth than the C-band Sentinel-1 observations (El Hajj et al., 2019; Entekhabi et al., 2010a). Furthermore, Gruber et al. (2020) points out that coarse scale products often better match local SMC dynamics than downscaled (finer) products. The result here does, however, not necessarily apply to other regions. The study region is rather flat and homogeneous regarding soil characteristics and meteorological conditions, so large regional differences in SMC dynamics are not expected. Moreover, information at field scale is still required in specific situations, such as after irrigation practices or in the presence of local drainage systems.

The SMAP retrievals are available for (part of) the SMC monitoring stations that provided the references for validating the Sentinel-1 IEM and TV-IEM SMC retrievals. One period in which the Sentinel-1 SMC retrievals significantly deviate from the references is the end of the 2018 summer, which is shown in more detail with the examples in Figs. 14 and 15. Whereas the SMC references remain low, the retrievals show an increased SMC level especially from mid-August. The same is visible in the SMAP retrievals (Chan et al., 2018, 2016; Van der Velde et al., 2021). At the end of July and in August 2018 a number of rainfall events occurred, but the 2018 summer was exceptionally dry in the months before and these rainfall events are not or only minorly reflected in the SMC references. The SMC references originate from measurements at $5\,\mathrm{cm}$ depth and due to the extreme dryness of the soil and high evaporative demand (Van der Velde et al., 2021), we expect that (most of) the rainfall did not fully infiltrate the sensor's influence zone of $1\,\mathrm{cm}$ to $9\,\mathrm{cm}$ soil depth. Field V is located in a slightly wetter area than field II and the level of the SMC references increased from
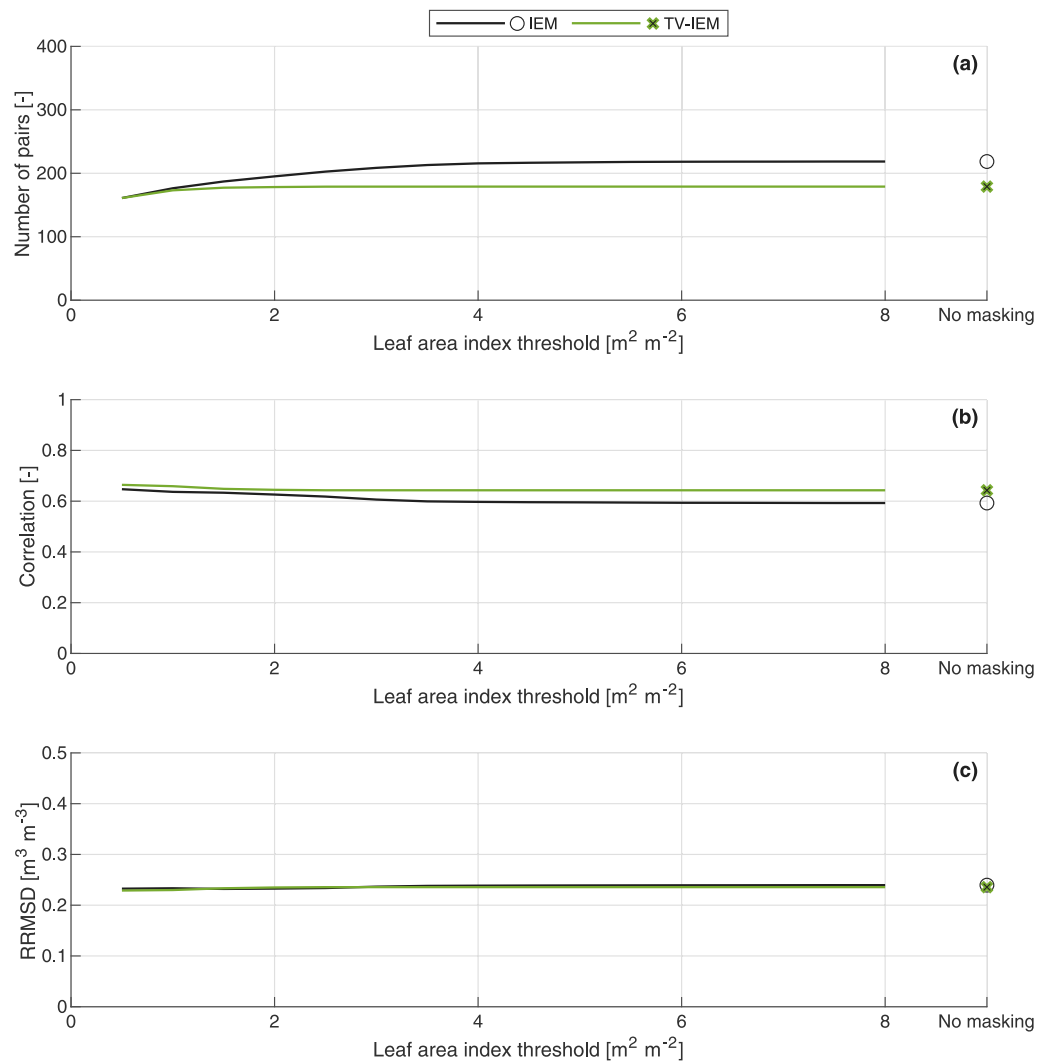
Fig. 13. Performance metric means of the study fields, after first applying variant 2 from Section 5.3.2, for a range of LAI thresholds used to mask the SMC retrievals. Only the SMC retrievals for which a Sentinel-2 LAI estimate was available are included.

the end of August. Still, in this period the SMC retrievals show more dynamics in response to the rainfall than the references.

Rainfall does not explain all of the increased SMC retrievals, as can be seen in July, beginning of August, mid-September and mid-October in Figs. 14 and 15. Also the SMAP retrievals remain low in these periods, which indicates an issue in the Sentinel-1 SMC retrievals. The increased SMC retrievals originate from Sentinel-1 σ^0 observations acquired in orbits 88 & 139 (see Supplement 5). The σ^0 observations acquired in orbits 88 & 139 have an incidence angle of 40.8° to 45.6°, whereas the σ^0 observations from orbits 15 & 37 have an incidence angle of 32.3° to 37.8° (Table 3). For larger incidence angles, the microwaves have a longer path through the vegetation to and from the soil surface and, consequently, experience more effect of vegetation and a lower sensitivity to SMC (e.g. Crow et al., 2010; Palmisano et al., 2018; Ulaby et al., 1979). This is also seen in the TV simulations, discussed in Section 3. The higher σ^0 to SMC sensitivity for lower incidence angles is reflected in better SMC retrieval performance metrics for orbits 15 & 37 than for orbits 88 & 139, shown in Fig. S14 and summarized in Table 7.

5.4.3. Note on the use of multiple products

SMC retrievals are generally evaluated against in situ references to quantify their performance. From the comparison of the IEM and TV-IEM SMC retrievals against SMAP 9 km retrievals, it was inferred that

rainfall did not fully infiltrate the influence zone of the in situ sensors at 5 cm depth in the months after the exceptionally dry 2018 summer. The satellite retrievals and the in situ sensors provide information for different soil layers, as was also found for e.g. SMOS (Rondinelli et al., 2015; Escorihuela et al., 2010) and SMAP retrievals (Van der Velde et al., 2021; Shellito et al., 2016). Besides, the comparison pointed to increased SMC retrievals from two Sentinel-1 orbits.

Furthermore, the two scheme implementations (without and with the vegetation correction) and the SMC products to which their performances were compared are based on imagery from different satellites or on different algorithms. As a consequence, the individual retrievals of these products are different. However, the performance metrics indicate that all these SMC products provide information about SMC at field scale. It would, therefore, be interesting to research the representation of field-scale SMC as an ensemble of SMC products. Ensemble representations provide multiple predictions of a quantity for the same time and location, based on multiple models, initial condition, forcing and/or parameter uncertainties. These are common practice in other fields, such as for meteorological forecasts (e.g. Buizza et al., 2005; Bougeault et al., 2010) and river discharge forecasts (e.g. Cloke and Pappenberger, 2009; Fleming et al., 2015; He et al., 2009). SMC retrievals have in common with meteorological and river discharge forecasts that they are uncertain. Ensembles of SMC retrievals could reveal the uncertainties and provide information on the possibility of a

Table 6
The performance of other SMC products from satellite imagery.

| Study	Product	r_P [–]	$RRMSD$ [–]	Evaluation
El Hajj et al. (2017)	Sentinel-1 VV, IEM combined with the WCM for incorporating vegetation effects. Field-scale product.	not reported	0.25	The averages of 25 to 30 measurements within a study field were used as references. The reported $RMSD$ values were unbiased, using Eq. (3) in Entekhabi et al. (2010b), with the also reported mean bias. The $RRMSD$ was calculated from this and reported SMC ranges.
	The first product and a priori information on SMC (wet/dry).	not reported	0.18	
Carranza et al. (2019)	Sentinel-1 VV, change detection method for a field-scale product. We subjected the retrievals to CDF matching.	0.44	0.25	Evaluated against the measurements from single stations.
Bazzi et al. (2019)	First product of El Hajj et al. (2017), at 1 km resolution. We subjected the retrievals to CDF matching.	0.78	0.15	The references from El Hajj et al. (2017) were used, averaged for the fields within 1 km by 1 km grid cells.
	The 1 km resolution Copernicus Surface Soil Moisture product, developed by Bauer-Marschallinger et al. (2019). We subjected the retrievals to CDF matching.	0.43	0.23	
Balenzano et al. (2021)	Sentinel-1, short term change detection approach for a 1 km resolution product. We subjected the retrievals to CDF matching.	0.70	0.14	The 1 km resolution product was evaluated at 1.6 km × 1.6 km by averaging the SMC retrievals and references from 11 stations that cover this area.
Pezij et al. (2020)	SMAP 9 km product (SCA-V morning overpasses). We subjected the retrievals to CDF matching.	0.77	0.16	The SMAP product (Chan et al., 2018) was extracted for the study region. Evaluated against the measurements from single stations (i.e. at field scale): stations 2, 3, 4, 5, 11, 13, 14, 15, 16, 17, 18 and 19.
Van der Velde et al. (2021)	SMAP 36 km product (SCA-V). We subjected the retrievals to CDF matching.	0.78	0.15	The SMAP product (Chan et al., 2016) was extracted for the study region, specifically SMAP reference pixel 3606. Evaluated against the measurements from single stations (i.e. field scale) in SMAP reference pixel 3606: stations 2, 3, 5, 11, 15, 16, 17.
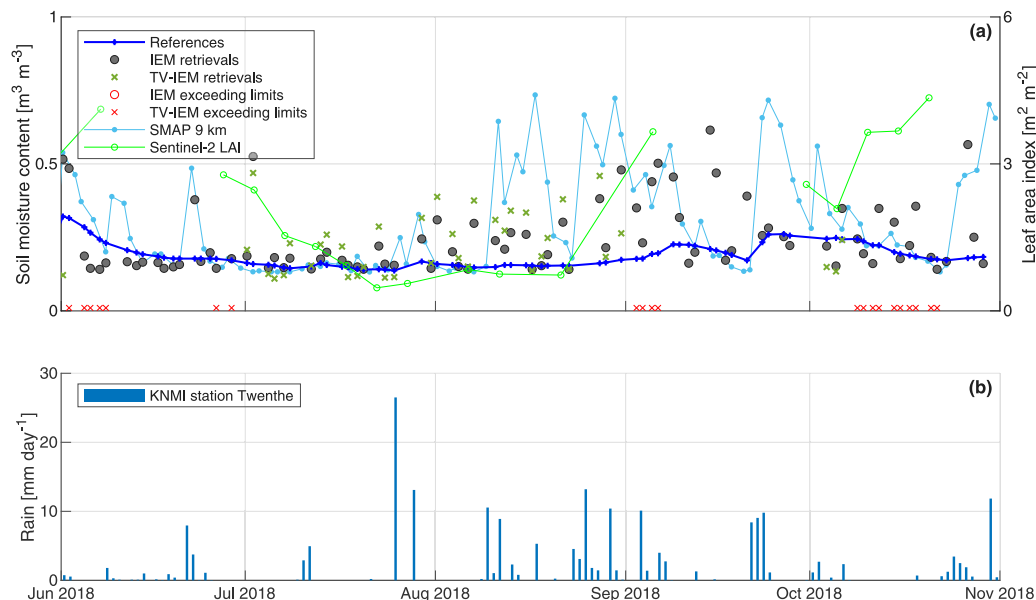
Fig. 14. SMC retrievals and references for field V during the 2018 summer. Field V has the best $RRMSD$ retrieval performance after fields XVIII and XVII, for which no references are available in this period. The SMAP 9 km retrievals for the pixel in which field V is located are shown. Both the Sentinel-1 and SMAP SMC retrievals were CDF-matched against the references over the complete time period (25 November 2015 to 1 November 2018). The rainfall data originate from the weather station Twenthe, which is operated by the Royal Netherlands Meteorological Institute ('Koninklijk Nederlands Meteorologisch Instituut' in Dutch, or KNMI; KNMI, 2019).
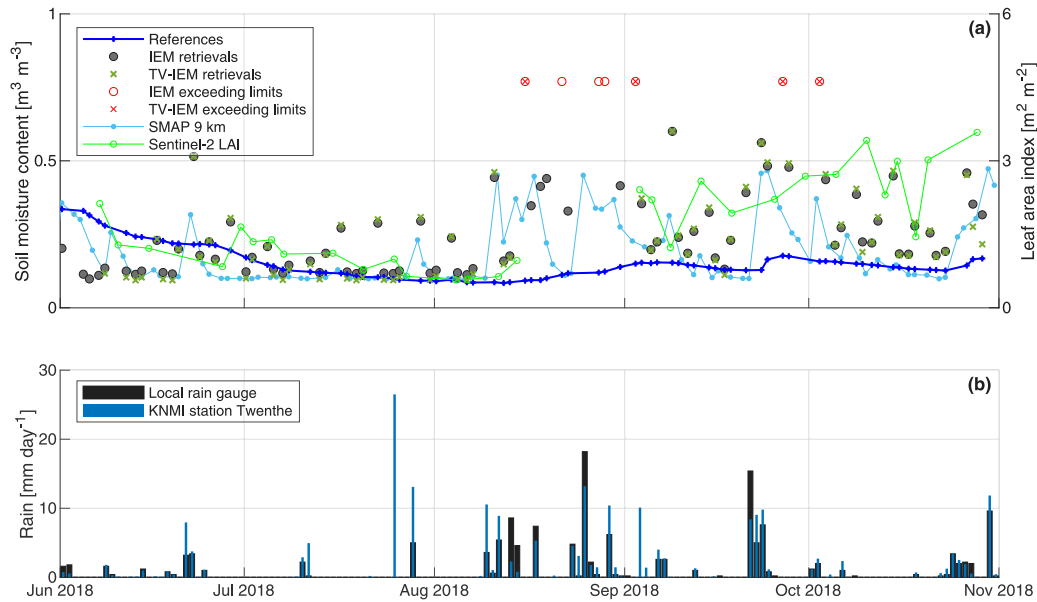
Fig. 15. Same as Fig. 14, but for field II. The rainfall data originate from the weather station Twenthe (KNMI, 2019) and from a local rain gauge adjacent to field II.

Table 7
Performance metrics means of the study fields, for the SMC retrievals from Sentinel-1 σ^0 observations acquired in orbits 15 & 37 and in orbits 88 & 139. The performance metrics per study field are shown in Fig. S14.

SMC product	Orbits	Number of pairs	r_P [–]	$RMSD$ [m^3 m^{-3}]	$RRMSD$ [–]
IEM all retrievals	All	322.9	0.46	0.14	0.25
	15 & 37	162.4	0.52	0.13	0.24
	88 & 139	160.4	0.41	0.15	0.29
TV-IEM	All	164.9	0.56	0.13	0.25
	15 & 37	82.3	0.63	0.12	0.23
	88 & 139	82.5	0.47	0.14	0.29

certain (e.g. extreme) SMC condition to occur. SMC products that could be validated are the 500 m product from Sentinel-1 imagery retrieved with a multi-temporal algorithm (Pulvirenti et al., 2018), the 1 km Copernicus Surface Soil Moisture product from Sentinel-1 imagery with a change detection algorithm (Bauer-Marschallinger et al., 2019), the 1 km product from Sentinel-1 imagery with the short term change detection algorithm (Balenzano et al., 2021), the 1 km and 3 km products from a combination of SMAP and Sentinel-1 imagery (Das et al., 2019), and several more, and potentially be included in an ensemble of SMC products.

The comparison of the IEM and TV-IEM SMC retrievals against other SMC products illustrated that the SMC estimates from satellites and from in situ sensors provide information for different soil layers and, in an optimum setting, complement each other. Besides, it was demonstrated that such an analysis of multiple SMC products in conjunction may provide further insights into these products. Lastly, ensembles of SMC retrievals could reveal the uncertainties and show the probability of SMC conditions.

6. Conclusions

An operationally applicable scheme is presented for field-scale SMC retrieval over meadows from SAR σ^0 observations, and this scheme is evaluated without (IEM) and with vegetation correction (TV-IEM). The TV vegetation scattering and absorption model and the IEM surface scattering model were parameterized for grass-covered soil surfaces using input data sets that are regionally available — with global alternatives — and parameters available from other sources. To facilitate fast inversion of σ^0 observations to SMC, look-up tables of the TV-IEM-modelled direct vegetation σ^0 (σ_v^0), σ^0 from soil–vegetation pathways (σ_{sv}^0), soil surface σ^0 (σ_s^0) and the vegetation two-way transmissivity

(γ^2) were generated on fine grids. The axes of these look-up tables are incidence angle, LAI, VWC and SMC. We used the look-up tables to invert field-averaged Sentinel-1 σ^0 observations into SMC for meadows. Field-scale LAI information was derived from a Sentinel-2 vegetation product.

The Sentinel-2 LAI estimates were validated against in situ measurements collected on two meadows and four maize fields. The r_Ps are 0.93 and 0.63 for the meadows and the maize fields, respectively, the $RMSD$s are 1.11 m^2 m^{-2} and 0.83 m^2 m^{-2}, and both $uRMSD$s are 0.82 m^2 m^{-2}. The results demonstrate that the Sentinel-2 LAI product provides field-scale information. However, despite the rather good performance, the Sentinel-2 LAI uncertainty of 0.82 m^2 m^{-2} results in the lower LAI range in many invalid SMC retrievals because the modelled σ^0 to SMC relation is very sensitive to LAI and in the upper LAI range it propagates into large SMC retrieval deviations because the σ^0 to SMC sensitivity diminishes.

The SMC retrieval scheme was demonstrated by retrieving the SMC for 21 meadows and validating the results against references from adjacent in situ monitoring stations. By setting the SMC retrievals that exceed the upper retrieval limit of 0.75 m^3 m^{-3} during the wet period to the maximum SMC, the performance metrics improve to mean r_Ps of 0.55 for IEM and 0.64 for TV-IEM, $RMSD$s of 0.14 m^3 m^{-3} for IEM and 0.13 m^3 m^{-3} for TV-IEM, and $RMSD$s relative to the range of the SMC references ($RRMSD$) of 0.24 for both IEM and TV-IEM. Masking the SMC retrievals for dense vegetation also improves the performance metrics, but this is a trade-off with the number of retrievals. Because not for every Sentinel-1 σ^0 observation a Sentinel-2 LAI estimate is available and TV-IEM results in more invalid SMC retrievals under dense vegetation conditions, more SMC retrievals are possible without the vegetation correction. By considering the same retrieval–reference pairs as for TV-IEM, the performance metrics of the SMC retrievals that

are obtained with IEM are practically equal to the performance metrics of the SMC retrievals with TV-IEM.

The assumed vegetation and surface roughness parameters probably degrade the performance of the SMC retrieval scheme. Regarding the vegetation parameters, values calibrated on an alpine meadow landscape were adopted from Dente et al. (2014). Results indicate that the vegetation correction may benefit from a calibration of the vegetation parameters. Regarding the surface roughness parameters, the results in Benninga et al. (2020) suggest that using a single set of surface roughness parameters is permitted for meadows across a larger region and multiple seasons. This finding was obtained for two meadows over two winter seasons. The results in this paper indicate that the used parameters provide a reasonable (initial) representation of meadows' surface roughness. The paper focuses on establishing a scheme for operational SMC retrieval and investigates whether, with the described implementation, the vegetation correction improves the SMC retrievals. Interesting further research questions are if SMC retrieval performance would improve with (i) a region-specific calibration of vegetation parameters, (ii) field-specific vegetation and roughness parameters, and (iii) how either can be established in a SMC retrieval scheme that is operationally applicable.

The IEM and TV-IEM retrieval performances are practically equal as well as are similar to the performances of two other Sentinel-1 based products at field scale, of which one was obtained with a data-driven (change detection) method and one with a semi-empirical vegetation model (WCM) combined with IEM. The SMAP $36 \, \text{km}$ and $9 \, \text{km}$ products perform better at the field scale, with mean $RRMSD$s of 0.15 and 0.16 respectively, but they may be unsuitable if larger regional differences are present and in field-specific situations such as after irrigation practices or with local drainage systems. From the comparison against other SMC products followed that analysing multiple SMC products in conjunction may provide further insights into these products, and ensembles of SMC retrievals could reveal the uncertainties and show the probability of SMC conditions.

CRediT authorship contribution statement

Harm-Jan F. Benninga: Conceptualization, Methodology, Software, Formal analysis, Investigation, Resources, Data curation, Writing – original draft, Writing – review & editing, Visualization. **Rogier van der Velde:** Conceptualization, Methodology, Validation, Investigation, Resources, Data curation, Writing – review & editing, Supervision, Project administration, Funding acquisition. **Zhongbo Su:** Conceptualization, Resources, Writing – review & editing, Supervision, Project administration, Funding acquisition.

Declaration of competing interest

The authors declare that they have no known competing financial interests or personal relationships that could have appeared to influence the work reported in this paper.

Data availability

Tables of processed Sentinel-1 σ^0 observations, masks for weather-related surface conditions, processed Sentinel-2 LAI estimates, SMC references, and the IEM and TV-IEM retrievals, as well as supplementary time series figures for the 21 study fields are available at https://doi.org/10.17026/dans-xcy-gza5 (Benninga et al., 2022). The Sentinel-1 images were downloaded from the Copernicus Open Access Hub (https://scihub.copernicus.eu/; Copernicus, 2019), the KNMI meteorological measurements were obtained from http://www.knmi.nl/nederland-nu/klimatologie-metingen-en-waarnemingen (KNMI, 2019), and V102 vegetation indicator maps and scene classifications were downloaded from the VITO Product Distribution Portal (VITO, 2019). The SMC references were collected by the Twente network, which is

operated by the Faculty of Geo-Information Science and Earth Observation (ITC) - University of Twente (Van der Velde et al., submitted for publication; Van der Velde and Benninga, 2022). The LAI measurements collected inside two meadows and five maize fields and the Sentinel-2 LAI estimates for these fields are available at https://doi.org/10.17026/dans-xxv-sdez (Benninga et al., 2021). The datasets at Benninga et al. (2021) and Benninga et al. (2022) contain modified Copernicus Sentinel data [2015–2019].

Appendix A. Supplementary data

Supplementary material related to this article can be found online at https://doi.org/10.1016/j.rse.2022.113191.

References

Actueel Hoogtebestand Nederland, 2012. Actueel Hoogtebestand Nederland. Version 2. Dataset. Available online: http://www.ahn.nl (accessed on 11 February 2019).

Altese, E., Bolognani, O., Mancini, M., Troch, P.A., 1996. Retrieving soil moisture over bare soil from ERS 1 synthetic aperture radar data: Sensitivity analysis based on a theoretical surface scattering model and field data. Water Resour. Res. 32 (3), 653–661. http://dx.doi.org/10.1029/95WR03638.

Amazirh, A., Merlin, O., Er-Raki, S., Gao, Q., Rivalland, V., Malbeteau, Y., Khabba, S., Escorihuela, M.J., 2018. Retrieving surface soil moisture at high spatio-temporal resolution from a synergy between Sentinel-1 radar and Landsat thermal data: A study case over bare soil. Remote Sens. Environ. 211, 321–337. http://dx.doi.org/10.1016/j.rse.2018.04.013.

Attema, E.P.W., Ulaby, F.T., 1978. Vegetation modeled as a water cloud. Radio Sci. 13 (2), 357–364. http://dx.doi.org/10.1029/RS013i002p00357.

Baghdadi, N., King, C., Chanzy, A., Wigneron, J.P., 2002. An empirical calibration of the integral equation model based on SAR data, soil moisture and surface roughness measurement over bare soils. Int. J. Remote Sens. 23 (20), 4325–4340. http://dx.doi.org/10.1080/01431160110107671.

Bakke, S.J., Ionita, M., Tallaksen, L.M., 2020. The 2018 northern European hydrological drought and its drivers in a historical perspective. Hydrol. Earth Syst. Sci. 24 (11), 5621–5653. http://dx.doi.org/10.5194/hess-24-5621-2020.

Balenzano, A., Mattia, F., Satalino, G., Lovergine, F.P., Palmisano, D., Peng, J., Marzahn, P., Wegmüller, U., Cartus, O., Dąbrowska-Zielińska, K., Musial, J.P., Davidson, M.W.J., Pauwels, V.R.N., Cosh, M.H., McNairn, H., Johnson, J.T., Walker, J.P., Yueh, S.H., Entekhabi, D., Kerr, Y.H., Jackson, T.J., 2021. Sentinel-1 soil moisture at 1 km resolution: A validation study. Remote Sens. Environ. 263, 112554. http://dx.doi.org/10.1016/j.rse.2021.112554.

Balenzano, A., Mattia, F., Satalino, G., Ouellette, J., Johnson, J.T., 2012. An experimental and theoretical study on the sensitivity of cross-polarized backscatter to soil moisture. In: 2012 IEEE Int. Geosci. Remote Sens. Symp.. Munich, Germany, pp. 3411–3414. http://dx.doi.org/10.1109/IGARSS.2012.6350688.

Bauer-Marschallinger, B., Freeman, V., Cao, S., Paulik, C., Schaufler, S., Stachl, T., Modanesi, S., Massari, C., Ciabatta, L., Brocca, L., Wagner, W., 2019. Toward global soil moisture monitoring with Sentinel-1: Harnessing assets and overcoming obstacles. IEEE Trans. Geosci. Remote Sens. 57 (1), 520–539. http://dx.doi.org/10.1109/TGRS.2018.2858004.

Bazzi, H., Baghdadi, N., El Hajj, M., Zribi, M., Belhouchette, H., 2019. A comparison of two soil moisture products S^{2}MP and Copernicus-SSM over Southern France. IEEE J. Sel. Top. Appl. Earth Obs. Remote Sens. 12 (9), 3366–3375. http://dx.doi.org/10.1109/jstars.2019.2927430.

Benninga, H.F., 2022. Estimation of field-scale soil moisture content and its uncertainties using Sentinel-1 satellite imagery. (Ph.D. thesis). University of Twente, http://dx.doi.org/10.3990/1.9789036553384, Chap. 4.

Benninga, H.F., Carranza, C.D.U., Pezij, M., Van Santen, P., Van der Ploeg, M.J., Augustijn, D.C.M., Van der Velde, R., 2018. The Raam regional soil moisture monitoring network in the Netherlands. Earth Syst. Sci. Data 10 (1), 61–79. http://dx.doi.org/10.5194/essd-10-61-2018.

Benninga, H.F., Van der Velde, R., Su, Z., 2019. Impacts of radiometric uncertainty and weather-related surface conditions on soil moisture retrievals with Sentinel-1. Remote Sens. 11 (17), 2025. http://dx.doi.org/10.3390/rs11172025.

Benninga, H.F., Van der Velde, R., Su, Z., 2020. Sentinel-1 soil moisture content and its uncertainty over sparsely vegetated fields. J. Hydrol. X 9, 100066. http://dx.doi.org/10.1016/j.hydroa.2020.100066.

Benninga, H.F., Van der Velde, R., Su, Z., 2021. Leaf area index field measurements. Dataset. http://dx.doi.org/10.17026/dans-xxv-sdez, DANS.

Benninga, H.F., Van der Velde, R., Su, Z., 2022. Supplementary data of 'Sentinel-1 soil moisture content retrieval over meadows using a physically based scattering model' (updated). Dataset. http://dx.doi.org/10.17026/dans-xcy-gza5, DANS.

Boé, J., Terray, L., Habets, F., Martin, E., 2007. Statistical and dynamical downscaling of the Seine basin climate for hydro-meteorological studies. Int. J. Climatol. 27 (12), 1643–1655. http://dx.doi.org/10.1002/joc.1602.

Bougeault, P., Toth, Z., Bishop, C., Brown, B., Burridge, D., Chen, D.H., Ebert, B., Fuentes, M., Hamill, T.M., Mylne, K., Nicolau, J., Paccagnella, T., Park, Y., Parsons, D., Raoult, B., Schuster, D., Dias, P.S., Swinbank, R., Takeuchi, Y., Tennant, W., Wilson, L., Worley, S., 2010. The THORPEX Interactive Grand Global Ensemble. Bull. Am. Meteorol. Soc. 91 (8), 1059–1072. http://dx.doi.org/10.1175/2010BAMS2853.1.

Bourbigot, M., Johnsen, H., Piantanida, R., Hajduch, G., Poullaouec, J., 2016. Sentinel-1 Product Definition (Document Number: S1-RS-MDA-52-7440). Technical Report, ESA, Available online: https://sentinel.esa.int/documents/247904/1877131/Sentinel-1-Product-Definition (accessed on 12 August 2019).

Bracaglia, M., Ferrazzoli, P., Guerriero, L., 1995. A fully polarimetric multiple scattering model for crops. Remote Sens. Environ. 54 (3), 170–179. http://dx.doi.org/10.1016/0034-4257(95)00151-4.

Brocca, L., Hasenauer, S., Lacava, T., Melone, F., Moramarco, T., Wagner, W., Dorigo, W., Matgen, P., Martínez-Fernández, J., Llorens, P., Latron, J., Martin, C., Bittelli, M., 2011. Soil moisture estimation through ASCAT and AMSR-E sensors: An intercomparison and validation study across Europe. Remote Sens. Environ. 115 (12), 3390–3408. http://dx.doi.org/10.1016/j.rse.2011.08.003.

Buitink, J., Swank, A.M., Van der Ploeg, M., Smith, N.E., Benninga, H.F., Van der Bolt, F., Carranza, C.D.U., Koren, G., Van der Velde, R., Teuling, A.J., 2020. Anatomy of the 2018 agricultural drought in the Netherlands using in situ soil moisture and satellite vegetation indices. Hydrol. Earth Syst. Sci. 24 (12), 6021–6031. http://dx.doi.org/10.5194/hess-24-6021-2020.

Buizza, R., Houtekamer, P.L., Pellerin, G., Toth, Z., Zhu, Y., Wei, M., 2005. A comparison of the ECMWF, MSC, and NCEP global ensemble prediction systems. Mon. Weather Rev. 133 (5), 1076–1097. http://dx.doi.org/10.1175/MWR2905.1.

Buras, A., Rammig, A., Zang, C.S., 2020. Quantifying impacts of the 2018 drought on European ecosystems in comparison to 2003. Biogeosciences 17 (6), 1655–1672. http://dx.doi.org/10.5194/bg-17-1655-2020.

Carranza, C., Benninga, H., Van der Velde, R., Van der Ploeg, M., 2019. Monitoring agricultural field trafficability using Sentinel-1. Agric. Water Manag. 224, 105698. http://dx.doi.org/10.1016/j.agwat.2019.105698.

Cenci, L., Pulvirenti, L., Boni, G., Chini, M., Matgen, P., Gabellani, S., Squicciarino, G., Pierdicca, N., 2017. An evaluation of Sentinel 1 for improving flash flood predictions via soil moisture-data assimilation. Adv. Geosci. 44, 89–100. http://dx.doi.org/10.5194/adgeo-44-89-2017.

Chan, S.K., Bindlish, R., O'Neill, P., Jackson, T., Njoku, E., Dunbar, S., Chaubell, J., Piepmeier, J., Yueh, S., Entekhabi, D., Colliander, A., Chen, F., Cosh, M.H., Caldwell, T., Walker, J., Berg, A., McNairn, H., Thibeault, M., Martínez-Fernández, J., Uldall, F., Seyfried, M., Bosch, D., Starks, P., Holifield Collins, C., Prueger, J., Van der Velde, R., Asanuma, J., Palecki, M., Small, E.E., Zreda, M., Calvet, J., Crow, W.T., Kerr, Y., 2018. Development and assessment of the SMAP enhanced passive soil moisture product. Remote Sens. Environ. 204, 931–941. http://dx.doi.org/10.1016/j.rse.2017.08.025.

Chan, S.K., Bindlish, R., O'Neill, P.E., Njoku, E., Jackson, T., Colliander, A., Chen, F., Burgin, M., Dunbar, S., Piepmeier, J., Yueh, S., Entekhabi, D., Cosh, M.H., Caldwell, T., Walker, J., Wu, X., Berg, A., Rowlandson, T., Pacheco, A., McNairn, H., Thibeault, M., Martínez-Fernández, J., González-Zamora, Á., Seyfried, M., Bosch, D., Starks, P., Goodrich, D., Prueger, J., Palecki, M., Small, E.E., Zreda, M., Calvet, J.C., Crow, W.T., Kerr, Y., 2016. Assessment of the SMAP passive soil moisture product. IEEE Trans. Geosci. Remote Sens. 54 (8), 4994–5007. http://dx.doi.org/10.1109/TGRS.2016.2561938.

Chiu, T., Sarabandi, K., 2000. Electromagnetic scattering from short branching vegetation. IEEE Trans. Geosci. Remote Sens. 38 (2), 911–925. http://dx.doi.org/10.1109/36.841974.

Cloke, H.L., Pappenberger, F., 2009. Ensemble flood forecasting: A review. J. Hydrol. 375 (3–4), 613–626. http://dx.doi.org/10.1016/j.jhydrol.2009.06.005.

Copernicus, 2019. Copernicus open access hub. Dataset. Available online: https://scihub.copernicus.eu/ (accessed on 28 June 2019).

Cosh, M.H., Jackson, T.J., Bindlish, R., Famiglietti, J.S., Ryu, D., 2005. Calibration of an impedance probe for estimation of surface soil water content over large regions. J. Hydrol. 311 (1–4), 49–58. http://dx.doi.org/10.1016/j.jhydrol.2005.01.003.

Cosh, M.H., Jackson, T.J., Starks, P., Heathman, G., 2006. Temporal stability of surface soil moisture in the Little Washita River watershed and its applications in satellite soil moisture product validation. J. Hydrol. 323 (1–4), 168–177. http://dx.doi.org/10.1016/j.jhydrol.2005.08.020.

Crow, W.T., Wagner, W., Naeimi, V., 2010. The impact of radar incidence angle on soil-moisture-retrieval skill. IEEE Geosci. Remote Sens. Lett. 7 (3), 501–505. http://dx.doi.org/10.1109/LGRS.2010.2040134.

Das, N.N., Entekhabi, D., Dunbar, R.S., Chaubell, M.J., Colliander, A., Yueh, S., Jagdhuber, T., Chen, F., Crow, W., O'Neill, P.E., Walker, J.P., Berg, A., Bosch, D.D., Caldwell, T., Cosh, M.H., Collins, C.H., Lopez-Baeza, E., Thibeault, M., 2019. The SMAP and Copernicus Sentinel 1A/B microwave active-passive high resolution surface soil moisture product. Remote Sens. Environ. 233, 111380. http://dx.doi.org/10.1016/j.rse.2019.111380.

Dente, L., Ferrazzoli, P., Su, Z., Van der Velde, R., Guerriero, L., 2014. Combined use of active and passive microwave satellite data to constrain a discrete scattering model. Remote Sens. Environ. 155, 222–238. http://dx.doi.org/10.1016/j.rse.2014.08.031.

Dente, L., Su, Z., Wen, J., 2012. Validation of SMOS soil moisture products over the Maqu and Twente regions. Sensors 12 (8), 9965–9986. http://dx.doi.org/10.3390/s120809965.

Dente, L., Vekerdy, Z., Su, Z., Ucer, M., 2011. Twente Soil Moisture and Soil Temperature Monitoring Network. Technical Report, Faculty of Geo-Information Science and Earth Observation (ITC), University of Twente, Enschede, the Netherlands, Available online: https://www.itc.nl/library/papers_2011/scie/dente_twe.pdf (accessed on 27 September 2018).

Draper, C.S., Walker, J.P., Steinle, P.J., de Jeu, R.A.M., Holmes, T.R.H., 2009. An evaluation of AMSR-E derived soil moisture over Australia. Remote Sens. Environ. 113 (4), 703–710. http://dx.doi.org/10.1016/j.rse.2008.11.011.

Drusch, M., Del Bello, U., Carlier, S., Colin, O., Fernandez, V., Gascon, F., Hoersch, B., Isola, C., Laberinti, P., Martimort, P., Meygret, A., Spoto, F., Sy, O., Marchese, F., Bargellini, P., 2012. Sentinel-2: ESA's optical high-resolution mission for GMES operational services. Remote Sens. Environ. 120, 25–36. http://dx.doi.org/10.1016/j.rse.2011.11.026.

Drusch, M., Wood, E.F., Gao, H., 2005. Observation operators for the direct assimilation of TRMM microwave imager retrieved soil moisture. Geophys. Res. Lett. 32 (15), L15403. http://dx.doi.org/10.1029/2005GL023623.

El Hajj, M., Baghdadi, N., Bazzi, H., Zribi, M., 2019. Penetration analysis of SAR signals in the C and L bands for wheat, maize, and grasslands. Remote Sens. 11 (1), 31. http://dx.doi.org/10.3390/rs11010031.

El Hajj, M., Baghdadi, N., Zribi, M., Angelliaume, S., 2016. Analysis of Sentinel-1 radiometric stability and quality for land surface applications. Remote Sens. 8 (5), 406. http://dx.doi.org/10.3390/rs8050406.

El Hajj, M., Baghdadi, N., Zribi, M., Bazzi, H., 2017. Synergic use of Sentinel-1 and Sentinel-2 images for operational soil moisture mapping at high spatial resolution over agricultural areas. Remote Sens. 9 (12), 1292. http://dx.doi.org/10.3390/rs9121292.

Entekhabi, D., Njoku, E.G., O'Neill, P., Kellogg, K.H., Crow, W.T., Edelstein, W.N., Entin, J.K., Goodman, S.D., Jackson, T.J., Johnson, J., Kimball, J., Piepmeier, J.R., Koster, R.D., Martin, N., McDonald, K.C., Moghaddam, M., Moran, S., Reichle, R., Shi, J.C., Spencer, M.W., Thurman, S.W., Tsang, L., Van Zyl, J., 2010a. The soil moisture active passive (SMAP) mission. Proc. IEEE 98 (5), 704–716. http://dx.doi.org/10.1109/JPROC.2010.2043918.

Entekhabi, D., Reichle, R.H., Koster, R.D., Crow, W.T., 2010b. Performance metrics for soil moisture retrievals and application requirements. J. Hydrometeorol. 11 (3), 832–840. http://dx.doi.org/10.1175/2010JHM1223.1.

Escorihuela, M.J., Chanzy, A., Wigneron, J.P., Kerr, Y.H., 2010. Effective soil moisture sampling depth of L-band radiometry: A case study. Remote Sens. Environ. 114 (5), 995–1001. http://dx.doi.org/10.1016/j.rse.2009.12.011.

European Space Agency (ESA), 2019. Sentinel application platform (SNAP) V6.0. Available online: http://step.esa.int (accessed on 8 April 2019).

FAO/IIASA/ISRIC/ISS-CAS/JRC, 2009. Harmonized world soil database. Dataset. FAO, Rome, Italy and IIASA, Laxenburg, Austria, Available online: https://www.fao.org/soils-portal/data-hub/soil-maps-and-databases/harmonized-world-soil-database-v12/en/ (accessed on 29 March 2022).

Fascetti, F., Pierdicca, N., Pulvirenti, L., 2017. Empirical fitting of forward backscattering models for multitemporal retrieval of soil moisture from radar data at L-band. J. Appl. Remote Sens. 11 (1), 016002. http://dx.doi.org/10.1117/1.jrs.11.016002.

Fleming, S.W., Bourdin, D.R., Campbell, D., Stull, R.B., Gardner, T., 2015. Development and operational testing of a super-ensemble artificial intelligence flood-forecast model for a Pacific northwest river. J. Am. Water Resour. Assoc. 51 (2), 502–512. http://dx.doi.org/10.1111/jawr.12259.

Flemish Institute for Technological Research (VITO), 2019. VITO product distribution portal. Dataset. Available online: https://www.vito-eodata.be/PDF/portal/Application.html (accessed on 17 September 2019).

Flemish Institute for Technological Research (VITO), 2022. WorldCover. Dataset. Available online: https://esa-worldcover.org/en (accessed on 29 March 2022).

Fung, A.K., Li, Z., Chen, K.S., 1992. Backscattering from a randomly rough dielectric surface. IEEE Trans. Geosci. Remote Sens. 30 (2), 356–369. http://dx.doi.org/10.1109/36.134085.

Gruber, A., De Lannoy, G., Albergel, C., Al-Yaari, A., Brocca, L., Calvet, J.C., Colliander, A., Cosh, M., Crow, W., Dorigo, W., Draper, C., Hirschi, M., Kerr, Y., Konings, A., Lahoz, W., McColl, K., Montzka, C., Muñoz-Sabater, J., Peng, J., Reichle, R., Richaume, P., Rüdiger, C., Scanlon, T., Van der Schalie, R., Wigneron, J.P., Wagner, W., 2020. Validation practices for satellite soil moisture retrievals: What are (the) errors? Remote Sens. Environ. 244, 111806. http://dx.doi.org/10.1016/j.rse.2020.111806.

He, Y., Wetterhall, F., Cloke, H.L., Pappenberger, F., Wilson, M., Freer, J., McGregor, G., 2009. Tracking the uncertainty in flood alerts driven by grand ensemble weather predictions. Meteorol. Appl. 16 (1), 91–101. http://dx.doi.org/10.1002/met.132.

Hornacek, M., Wagner, W., Sabel, D., Truong, H.L., Snoeij, P., Hahmann, T., Diedrich, E., Doubková, M., 2012. Potential for high resolution systematic global surface soil moisture retrieval via change detection using Sentinel-1. IEEE J. Sel. Top. Appl. Earth Obs. Remote Sens. 5 (4), 1303–1311. http://dx.doi.org/10.1109/JSTARS.2012.2190136.

Joseph, A.T., Van der Velde, R., O'Neill, P.E., Lang, R., Gish, T., 2010. Effects of corn on C- and L-band radar backscatter: A correction method for soil moisture retrieval. Remote Sens. Environ. 114 (11), 2417–2430. http://dx.doi.org/10.1016/j.rse.2010.05.017.

Justice, C.O., Townshend, J.R.G., Vermote, E.F., Masuoka, E., Wolfe, R.E., Saleous, N., Roy, D.P., Morisette, J.T., 2002. An overview of MODIS land data processing and product status. Remote Sens. Environ. 83 (1–2), 3–15. http://dx.doi.org/10.1016/S0034-4257(02)00084-6.

Kerr, Y.H., Al-Yaari, A., Rodriguez-Fernandez, N., Parrens, M., Molero, B., Leroux, D., Bircher, S., Mahmoodi, A., Mialon, A., Richaume, P., Delwart, S., Al Bitar, A., Pellarin, T., Bindlish, R., Jackson, T.J., Rüdiger, C., Waldteufel, P., Mecklenburg, S., Wigneron, J.P., 2016. Overview of SMOS performance in terms of global soil moisture monitoring after six years in operation. Remote Sens. Environ. 180, 40–63. http://dx.doi.org/10.1016/j.rse.2016.02.042.

Kim, S.B., Moghaddam, M., Tsang, L., Burgin, M., Xu, X., Njoku, E.G., 2014. Models of L-band radar backscattering coefficients over global terrain for soil moisture retrieval. IEEE Trans. Geosci. Remote Sens. 52 (2), 1381–1396. http://dx.doi.org/10.1109/TGRS.2013.2250980.

Knyazikhin, Y., Glassy, J., Privette, J.L., Tian, Y., Lotsch, A., Zhang, Y., Wang, Y., Morisette, J.T., Votava, P., Myneni, R.B., Nemani, R.R., Running, S.W., 1999. MODIS Leaf Area Index (LAI) and Fraction of Photosynthetically Active Radiation Absorbed by Vegetation (FPAR) Product (MOD15) Algorithm Theoretical Basis Document. Technical Report, Available online: https://modis.gsfc.nasa.gov/data/atbd/atbd_mod15.pdf (accessed on 9 October 2019).

Kornelsen, K.C., Coulibaly, P., 2013. Advances in soil moisture retrieval from synthetic aperture radar and hydrological applications. J. Hydrol. 476, 460–489. http://dx.doi.org/10.1016/j.jhydrol.2012.10.044.

Kornelsen, K.C., Coulibaly, P., 2015. Reducing multiplicative bias of satellite soil moisture retrievals. Remote Sens. Environ. 165, 109–122. http://dx.doi.org/10.1016/j.rse.2015.04.031.

Lei, F., Crow, W.T., Kustas, W.P., Dong, J., Yang, Y., Knipper, K.R., Anderson, M.C., Gao, F., Notarnicola, C., Greifeneder, F., McKee, L.M., Alfieri, J.G., Hain, C., Dokoozlian, N., 2020. Data assimilation of high-resolution thermal and radar remote sensing retrievals for soil moisture monitoring in a drip-irrigated vineyard. Remote Sens. Environ. 239, 111622. http://dx.doi.org/10.1016/j.rse.2019.111622.

LI-COR, 1992. LAI-2000 Plant Canopy Analyzer. Technical Report, LI-COR, Inc., Lincoln, NE USA, Available online: https://www.licor.com/env/support/LAI-2000/home.html (accessed on 9 October 2019).

LI-COR, 2004. FV2000 V1.0. The LAI-2000 data file viewer. LI-COR, Inc.. Lincoln, NE USA.

Mahanama, S.P.P., Koster, R.D., Reichle, R.H., Zubair, L., 2008. The role of soil moisture initialization in subseasonal and seasonal streamflow prediction - A case study in Sri Lanka. Adv. Water Resour. 31 (10), 1333–1343. http://dx.doi.org/10.1016/j.advwatres.2008.06.004.

Massey, F.J., 1951. The Kolmogorov-Smirnov test for goodness of fit. J. Amer. Statist. Assoc. 46 (253), 68–78. http://dx.doi.org/10.1080/01621459.1951.10500769.

METER Group, 2019. 5TM. Technical Report, METER Group, Inc., Pullman, WA USA, Available online: http://publications.metergroup.com/Manuals/20424_5TM_Manual_Web.pdf (accessed on 8 September 2021).

Ministry of Economic Affairs and Climate Policy, 2020. Basisregistratie Gewaspercelen. Dataset. Available online: https://www.pdok.nl/introductie/-/article/basisregistratie-gewaspercelen-brp- (accessed on 25 August 2021), Publieke Dienstverlening Op de Kaart.

Paepen, M., Wens, D., 2017. VITO Sentinel-2 Products User Manual. Technical Report, VITO, Available online: https://www.vito-eodata.be/PDF/image/VITO%20S2%20-%20Products_User_Manual_v1.0.pdf (accessed on 25 November 2021).

Palmisano, D., Balenzano, A., Satalino, G., Mattia, F., Pierdicca, N., Monti-Guarnieri, A., 2018. Sentinel-1 sensitivity to soil moisture at high incidence angle and its impact on retrieval. In: IGARSS 2018 - 2018 IEEE Int. Geosci. Remote Sens. Symp.. Valencia, Spain, pp. 1430–1433. http://dx.doi.org/10.1109/IGARSS.2018.8518613.

Paloscia, S., Pettinato, S., Santi, E., Notarnicola, C., Pasolli, L., Reppucci, A., 2013. Soil moisture mapping using Sentinel-1 images: Algorithm and preliminary validation. Remote Sens. Environ. 134, 234–248. http://dx.doi.org/10.1016/j.rse.2013.02.027.

Pathe, C., Wagner, W., Sabel, D., Doubkova, M., Basara, J.B., 2009. Using ENVISAT ASAR global mode data for surface soil moisture retrieval over Oklahoma, USA. IEEE Trans. Geosci. Remote Sens. 47 (2), 468–480. http://dx.doi.org/10.1109/TGRS.2008.2004711.

Pauwels, V.R.N., Hoeben, R., Verhoest, N.E.C., De Troch, F.P., 2001. The importance of the spatial patterns of remotely sensed soil moisture in the improvement of discharge predictions for small-scale basins through data assimilation. J. Hydrol. 251 (1–2), 88–102. http://dx.doi.org/10.1016/S0022-1694(01)00440-1.

Pellikaan, F., 2017. Grasseizoen 2017: lang, maar zonder groeispurt (in Dutch). Veeteelt Oct 2, 46–47, Available online: https://edepot.wur.nl/426132 (accessed on 25 November 2021).

Petropoulos, G.P., Ireland, G., Barrett, B., 2015. Surface soil moisture retrievals from remote sensing: Current status, products & future trends. Phys. Chem. Earth, Parts A/B/C 83–84, 36–56. http://dx.doi.org/10.1016/j.pce.2015.02.009.

Pezij, M., Augustijn, D.C.M., Hendriks, D.M.D., Hulscher, S.J.M.H., 2020. Applying transfer function-noise modelling to characterize soil moisture dynamics: A data-driven approach using remote sensing data. Environ. Model. Softw. 131, 104756. http://dx.doi.org/10.1016/j.envsoft.2020.104756.

Pezij, M., Augustijn, D.C.M., Hendriks, D.M.D., Weerts, A.H., Hummel, S., Van der Velde, R., Hulscher, S.J.M.H., 2019. State updating of root zone soil moisture estimates of an unsaturated zone metamodel for operational water resources management. J. Hydrol. X 4, 100040. http://dx.doi.org/10.1016/j.hydroa.2019.100040.

Piccard, I., Swinnen, E., De Keukelaere, L., Van De Kerchove, R., Eerens, H., 2020. Terrascope Sentinel-2 Algorithm Theoretical Base Document S2 - NDVI & BIOPAR - V200. Technical Report, VITO, Available online: https://docs.terrascope.be/DataProducts/Sentinel-2/references/VITO_S2_ATBD_S2_NDVI_BIOPAR_V200.pdf (accessed on 25 November 2021).

Pulvirenti, L., Squicciarino, G., Cenci, L., Boni, G., Pierdicca, N., Chini, M., Versace, C., Campanella, P., 2018. A surface soil moisture mapping service at national (Italian) scale based on Sentinel-1 data. Environ. Model. Softw. 102, 13–28. http://dx.doi.org/10.1016/j.envsoft.2017.12.022.

Reichle, R.H., Koster, R.D., 2004. Bias reduction in short records of satellite soil moisture. Geophys. Res. Lett. 31 (19), L19501. http://dx.doi.org/10.1029/2004GL020938.

Rondinelli, W.J., Hornbuckle, B.K., Patton, J.C., Cosh, M.H., Walker, V.A., Carr, B.D., Logsdon, S.D., 2015. Different rates of soil drying after rainfall are observed by the SMOS satellite and the South Fork in situ soil moisture network. J. Hydrometeorol. 16 (2), 889–903. http://dx.doi.org/10.1175/JHM-D-14-0137.1.

Royal Netherlands Meteorological Institute (KNMI), 2019. Klimatologie - metingen en waarnemingen. Dataset. Available online: http://www.knmi.nl/nederland-nu/klimatologie-metingen-en-waarnemingen (accessed on 7 April 2019).

Satalino, G., Mattia, F., Davidson, M.W.J., Le Toan, T., Pasquariello, G., Borgeaud, M., 2002. On current limits of soil moisture retrieval from ERS-SAR data. IEEE Trans. Geosci. Remote Sens. 40 (11), 2438–2447. http://dx.doi.org/10.1109/TGRS.2002.803790.

Schmidt, K., Tous Ramon, N., Schwerdt, M., 2018. Radiometric accuracy and stability of sentinel-1A determined using point targets. Int. J. Microw. Wirel. Technol. 10 (5–6), 538–546. http://dx.doi.org/10.1017/S1759078718000016.

Schwerdt, M., Schmidt, K., Tous Ramon, N., Klenk, P., Yague-Martinez, N., Prats-Iraola, P., Zink, M., Geudtner, D., 2017. Independent system calibration of Sentinel-1B. Remote Sens. 9 (6), 511. http://dx.doi.org/10.3390/rs9060511.

Shellito, P.J., Small, E.E., Colliander, A., Bindlish, R., Cosh, M.H., Berg, A.A., Bosch, D.D., Caldwell, T.G., Goodrich, D.C., McNairn, H., Prueger, J.H., Starks, P.J., Van der Velde, R., Walker, J.P., 2016. SMAP soil moisture drying more rapid than observed in situ following rainfall events. Geophys. Res. Lett. 43 (15), 8068–8075. http://dx.doi.org/10.1002/2016GL069946.

Singh, A., Gaurav, K., Meena, G.K., Kumar, S., 2020. Estimation of soil moisture applying modified Dubois model to Sentinel-1; A regional study from central India. Remote Sens. 12 (14), 2266. http://dx.doi.org/10.3390/rs12142266.

Stiles, J.M., Sarabandi, K., Ulaby, F.T., 2000. Electromagnetic scattering from grassland — Part II : Measurement and modeling results. IEEE Trans. Geosci. Remote Sens. 38 (1), 349–356. http://dx.doi.org/10.1109/36.823930.

Tesemma, Z.K., Wei, Y., Western, A.W., Peel, M.C., 2014. Leaf area index variation for crop, pasture, and tree in response to climatic variation in the Goulburn–Broken catchment, Australia. J. Hydrometeorol. 15 (4), 1592–1606. http://dx.doi.org/10.1175/JHM-D-13-0108.1.

Torres, R., Snoeij, P., Geudtner, D., Bibby, D., Davidson, M., Attema, E., Potin, P., Rommen, B., Floury, N., Brown, M., Traver, I.N., Deghaye, P., Duesmann, B., Rosich, B., Miranda, N., Bruno, C., L'Abbate, M., Croci, R., Pietropaolo, A., Huchler, M., Rostan, F., 2012. GMES Sentinel-1 mission. Remote Sens. Environ. 120, 9–24. http://dx.doi.org/10.1016/j.rse.2011.05.028.

Ulaby, F.T., Bradley, G.A., Dobson, M.C., 1979. Microwave backscatter dependence on surface roughness, soil moisture, and soil texture: Part II–Vegetation-covered soil. IEEE Trans. Geosci. Electron. 17 (2), 33–40. http://dx.doi.org/10.1109/TGE.1979.294626.

Ulaby, F.T., Long, D.G., 2014. Microwave Radar and Radiometric Remote Sensing, 1 The University of Michigan Press, Ann Arbor, MI USA.

Van der Velde, R., Benninga, H.F., 2022. Ten years profile soil moisture and temperature measurements in Twente (version 2022). Dataset. http://dx.doi.org/10.17026/dans-xr2-m6d8, DANS.

Van der Velde, R., Benninga, H.F., Retsios, B., 2022. Twelve years profile soil moisture and temperature measurements in Twente, the Netherlands. Earth Syst. Sci. Data Discuss. [preprint] http://dx.doi.org/10.5194/essd-2022-90.

Van der Velde, R., Colliander, A., Pezij, M., Benninga, H.F., Bindlish, R., Chan, S.K., Jackson, T.J., Hendriks, D.M.D., Augustijn, D.C.M., Su, Z., 2021. Validation of SMAP L2 passive-only soil moisture products using upscaled in situ measurements collected in Twente, the Netherlands. Hydrol. Earth Syst. Sci. 25 (1), 473–495. http://dx.doi.org/10.5194/hess-25-473-2021.

Van der Velde, R., Su, Z., 2009. Dynamics in land-surface conditions on the Tibetan Plateau observed by advanced synthetic aperture radar (ASAR). Hydrol. Sci. J. 54 (6), 1079–1093. http://dx.doi.org/10.1623/hysj.54.6.1079.

Van der Velde, R., Su, Z., Van Oevelen, P., Wen, J., Ma, Y., Salama, M.S., 2012. Soil moisture mapping over the central part of the Tibetan Plateau using a series of ASAR WS images. Remote Sens. Environ. 120, 175–187. http://dx.doi.org/10.1016/j.rse.2011.05.029.

Veeneman, W., Remmelink, G., Tjoonk, L., Van der Weiden, T., Philipsen, B., Van den Pol van Dasselaar, A., Stienezen, M., 2017. 2016 was uitstekend graslandjaar (in Dutch). V-Focus Feb, 24–26, Available online: https://edepot.wur.nl/426593 (accessed on 25 November 2021).

Vereecken, H., Huisman, J.A., Pachepsky, Y., Montzka, C., Van der Kruk, J., Bogena, H., Weihermüller, L., Herbst, M., Martinez, G., Vanderborght, J., 2014. On the spatio-temporal dynamics of soil moisture at the field scale. J. Hydrol. 516, 76–96. http://dx.doi.org/10.1016/j.jhydrol.2013.11.061.

Verhoest, N.E.C., Lievens, H., Wagner, W., Álvarez-Mozos, J., Moran, M.S., Mattia, F., 2008. On the soil roughness parameterization problem in soil moisture retrieval of bare surfaces from synthetic aperture radar. Sensors 8 (7), 4213–4248. http://dx.doi.org/10.3390/s8074213.

Vinnikov, K.Y., Robock, A., Qiu, S., Entin, J.K., 1999. Optimal design of surface networks for observation of soil moisture. J. Geophys. Res. Atmos. 104 (D16), 19743–19749. http://dx.doi.org/10.1029/1999JD900060.

Wagner, W., Naeimi, V., Scipal, K., De Jeu, R., Martínez-Fernández, J., 2007. Soil moisture from operational meteorological satellites. Hydrogeol. J. 15, 121–131. http://dx.doi.org/10.1007/s10040-006-0104-6.

Wang, Q., Van der Velde, R., Su, Z., 2018. Use of a discrete electromagnetic model for simulating Aquarius L-band active/passive observations and soil moisture retrieval. Remote Sens. Environ. 205, 434–452. http://dx.doi.org/10.1016/j.rse.2017.10.044.

Western, A.W., Grayson, R.B., Blöschl, G., 2002. Scaling of soil moisture: A hydrologic perspective. Annu. Rev. Earth Planet. Sci. 30, 149–180. http://dx.doi.org/10.1146/annurev.earth.30.091201.140434.

Wösten, J.H.M., De Vries, F., Hoogland, T., Massop, H.T.L., Veldhuizen, A.A., Vroon, H.R.J., Wesseling, J.G., Heijkers, J., Bolman, A., 2013. BOFEK2012, de nieuwe, bodemfysische schematisatie van Nederland (in Dutch). Technical Report, Alterra, Wageningen UR, Wageningen, the Netherlands, Available online: http://edepot.wur.nl/247678 (accessed on 27 September 2018).

Xiao, Z., Song, J., Yang, H., Sun, R., Li, J., 2022. A 250 m resolution global leaf area index product derived from MODIS surface reflectance data. Int. J. Remote Sens. 43 (4), 1409–1429. http://dx.doi.org/10.1080/01431161.2022.2039415.